

Supplementary Information for
Reversible regulation of thermal conductivity through spin-crossover transitions

Qichen Song¹, Rahil Ukani¹, Vidhya M. Dev¹, Hong Ki Kim¹, Jungwoo Shin², Jinyoung Seo¹, Caleb Stamper^{3,4}, Daniel W. Laorenza¹, Ryan D. McGillicuddy¹, Jason J. Calvin¹, Yukyung Moon¹, Catherine Thai¹, Jason D. Braun¹, Dehong Yu⁴, Gang Chen², Jarad A. Mason^{1*}

¹Department of Chemistry and Chemical Biology, Harvard University, Cambridge, MA 02138, USA

²Department of Mechanical Engineering, Massachusetts Institute of Technology, Cambridge, MA 02139, USA

³Institute for Superconducting and Electronic Materials, University of Wollongong, Wollongong, NSW 2500,
Australia

⁴Australian Nuclear Science and Technology Organisation, Lucas Heights, NSW 2234, Australia

Methods

Sample preparation

Bulk Fe[HB(tz)₃]₂ was synthesized according to a previously reported procedure²⁶. Afterwards, the Fe[HB(tz)₃]₂ powder was dissolved in ethanol at 80 °C. The resulting solution was then cooled at a rate of 4 °C per hour to room temperature (21 °C). Larger single crystals (~100 μm) formed after 72 hours. The crystals were deposited onto a Si substrate via drop-casting (Fig. S1). E-beam evaporation and sputtering techniques were used to deposit a 2-nm titanium adhesion layer followed by a 93-nm or 64-nm thin film of Au on the samples for the frequency-domain thermoreflectance measurements shown in Fig. 1 and Fig. 2, respectively. The thickness of the transducer layer was determined by atomic force microscopy (conducted on a Jupiter XR atomic force microscope). The electronic thermal conductivity, which dominates the total thermal conductivity of the transducer layer, was determined through four-point-probe measurements from 100 K to 300 K and was found to be 156 W m⁻¹ K⁻¹ and 97 W m⁻¹ K⁻¹ for the 93-nm and 64-nm films, respectively, at room temperature. Benchmark thermal conductivity measurements for samples with transducer layers using e-beam evaporation and sputtering techniques can be found in Ref.⁴⁶ and Fig. S15. Bulk Fe(Fpr-trz₂-dmpn)(NCS)₂ was synthesized according to Ref.⁴⁰, and single crystals were dispersed in ether and directly drop-cast on Si substrates, followed by sputtering of a 2-nm Ti adhesion layer and a 64-nm thin film of Au as the transducer layer.

Frequency-domain thermoreflectance (FDTR)

The FDTR instrument contains a fiber laser (Coherent OBIS LX 458 nm) with digital modulation as the pump and a continuous wave (CW) laser (Coherent OBIS LS 532 nm) as the probe. A rotational half-wave plate and quarter-wave plate (omitted in the schematic in Fig. 1 for clarity) were used to modulate the relative intensity of the reference and reflected probe beam in order to minimize their common noise. Afterwards, these two probe beams were sent to a balanced photodetector, and the detected signal was amplified by a lock-in amplifier (Zurich Instruments HF2LI). The ratio of the AC part divided by the DC part of the amplified signal was taken as the FDTR signal.

Silver paste was used to anchor the Si substrate onto the temperature stage to enhance heat dissipation. The pump and probe laser wavelength were 458 and 532 nm, respectively. The pump and probe power were set to be 1 mW and 3 mW (as measured by a Thorlabs PM100USB power meter), respectively, to minimize laser heating and the steady-state temperature rise (a constant temperature deviation from the background temperature) from the unmodulated part of the probe. The pump and probe laser radii were both around 3 μm, with the root-mean-square effective radius measured by the beam-offset method (Fig. S15a). Typically, the amplitude of the modulated temperature increases as the modulation frequency decreases. Hence, modest-to-high modulation frequencies (~1 MHz to ~10 MHz) for the pump laser were used to ensure that the phase transition is not triggered by the pump laser heating.

The sample thermal conductivity, κ , and the interfacial thermal conductance, G , between the sample and transducer layer were fitting variables when fitting the phase lag with the Fourier heat conduction model³⁰. In the model, the full anisotropic thermal conductivity tensor has been considered (Eq. S3). However, the sensitivity analysis suggests our measurement is only sensitive to the cross-plane thermal conductivity (Fig. S10). In the fitting process, we performed a non-linear least-square minimization of the residuals, defined by the difference between experimentally

obtained phase data and the phase computed using the Fourier heat conduction model. Error bars were calculated from Monte Carlo simulations, assuming each parameter follows a normal distribution with a 5% uncertainty. The formalism for the Monte Carlo simulation is adopted from a previous report⁴⁷.

Neutron scattering

The neutron scattering experiments were conducted on the time-of-flight cold-neutron spectrometer, Pelican, at the Australian Centre for Neutron Scattering—part of the Australian Nuclear Science and Technology Organisation (ANSTO)⁴⁸. The instrument was configured with an incident neutron wavelength of 4.69 Å, corresponding to an incident energy of 0.899 THz (3.72 meV) and an energy resolution of 0.033 THz (0.135 meV) at the elastic line.

A mass of 0.44 g of Fe[HB(tz)₃]₂ powder was placed in an aluminum plate sample holder with two aluminum spacers allowing for a uniform sample thickness of 0.4 mm resulting in an estimated neutron scattering ratio of ~10% (<90% transmission). Importantly, the calculated scattering ratio considers neutron absorption—a significant factor in our case due to the presence of boron, which has a large neutron absorption cross-section. Measurements were taken between 250 K and 400 K using a top-load cryo-furnace. A corresponding empty sample holder was measured in the same conditions as for the samples for background subtraction. In addition, a standard plate-shaped vanadium sample was also measured for detector efficiency normalization and energy resolution calibration. The generalized phonon density of states was obtained on the neutron energy gain side. The measurements were not corrected for multiple scattering.

Density-functional tight binding (DFTB) calculations

The extended tight-binding method with GFN1-xTB parameterizations⁴⁹ as implemented in the Amsterdam Modeling Suite (AMS) was used for DFTB calculations. 660 basis functions were used to construct the model Hamiltonian with periodic boundary conditions for the unit cell that contains 188 atoms. For geometry optimization, we started with the structure resolved from single-crystal X-ray diffraction (XRD)⁴¹, kept the unit cell dimensions fixed, and used the Quasi-Newton method to relax atomic positions within the unit cell (Fig. S26). The threshold for nuclear gradients as a convergence criterion of geometry optimization was set to 10⁻³ Hartree/Å.

The phonon normal modes at the Γ point were obtained by solving the eigenvalue problem, $\omega^2 e_i^\alpha = \sum_{j\beta} \frac{\Psi_{ij}^{\alpha\beta}}{\sqrt{m_i m_j}} e_j^\beta$, where ω is the phonon frequency, e_i^α is the phonon eigenvector, $\Psi_{ij}^{\alpha\beta} = \frac{\partial^2 E}{\partial R_i^\alpha \partial R_j^\beta}$ is the Harmonic force constant (also known as the Hessian matrix element) calculated using DFTB, E is the total energy, m_i is the mass of atom i and R_i^α is its Cartesian coordinate along the α -axis ($\alpha = x, y, z$). Fig. S30 shows the calculated phonon density of states, illustrating phonon redshifts similar to those presented in Fig. 4.

Anisotropic thermal conductivity

The unit cell of Fe[HB(tz)₃]₂ is anisotropic; thus, the thermal conductivity may be different along different crystallographic directions. However, the FDTR measurements performed are only sensitive to the cross-plane thermal conductivity. As illustrated in Fig. S10, the sensitivity of the phase of thermoreflectance to the in-plane thermal conductivity $\kappa_{||}$ is almost negligible. As a

consequence, the cross-plane thermal conductivity, κ_z , is primarily being measured along the (001) axis (Fig. S25). In the following, we use κ and κ_z interchangeably.

The importance of accurate evaluation of the lattice heat capacity

As shown in Fig. S10, the sensitivity of the FDTR fitting to thermal conductivity, κ_z , and volumetric heat capacity, C , is almost identical. This indicates that κ_z and C are almost perfectly anti-correlated, making it difficult to individually determine these parameters from the FDTR data fitting. Therefore, to accurately measure thermal conductivity, the lattice heat capacity must be independently measured using a method other than FDTR. Fig. S4 shows the temperature-dependent volumetric lattice heat capacity obtained from semi-adiabatic relaxation calorimetry and differential scanning calorimetry (DSC). Specifically, a Quantum Design Physical Property Measurement System (PPMS) was used to measure heat capacity as a function of temperature. For the PPMS heat capacity measurements, the sample was prepared following a literature procedure by mixing Cu foil with the sample (10.53 mg) and encasing the entire sample in copper foil to enhance the overall thermal conductivity of the sample, with a total Cu foil mass of 30.81 mg⁵⁰. Additionally, we performed a heat capacity measurement using a TA Instruments DSC2500 with heating rate of 20 °C/min following the ASTM test standard. The smeared peak in the DSC data can be attributed to thermal lag and sample geometry, and an ideal peak profile would be much sharper. Specifically, we underscore that in all DSC measurements, bulk samples are used, which consist a distribution of single crystals with varying dimensions and local environments. In contrast, we measure a single crystal in FDTR measurements.

It is therefore important to retrieve a baseline that accurately represents the intrinsic, sensible lattice heat capacity near the phase transition temperature. Here, we used a Debye model combined with a linear-in- T term to describe the lattice heat capacity, given by $C_p(T) = A \left(\frac{T}{T_D} \right)^3 \int_0^{T_D/T} \frac{x^4 e^x}{(e^x - 1)^2} dx + BT + C$, where A , B , C , and T_D are fitting constants. The reasons behind the choice of this functional form were two-fold. First, the same model accurately describes the features of the heat capacity of Co[HB(tz)₃]₂, which is isostructural to Fe[HB(tz)₃]₂ and does not have any phase transitions (Fig. S4). Second, the complex unit-cell structure of Fe[HB(tz)₃]₂ gives rise to many phonon modes that are gradually excited as the temperature rises. The linear-in- T term effectively captures the physical picture where new degrees of freedom—beyond just acoustic phonons represented by the Debye model—are continuously being excited. Specifically, we applied this model to the LS and HS phases separately, obtaining two sets of fitting constants. Fig. S5 illustrates that the baselines independently determined from PPMS and DSC measurements of heat capacity gave similar best fits for the thermal conductivity of both the low-spin (LS) and high-spin (HS) phases.

Low-thermal-conductivity alloy transducer

Benchmark measurements using a gold transducer layer from e-beam evaporation to verify the accuracy of the FDTR measurements can be found in prior work⁴⁶. Here, we performed additional measurements with a sample coated with a different composition transducer layer to validate our FDTR measurements. Generally, a metal transducer layer with a thermal conductivity lower than that of gold can boost the sensitivity of FDTR when fitting the thermal conductivity in samples with relatively low thermal conductivity. This is because the high thermal conductivity of the gold transducer layer minimizes the temperature gradient in the in-plane directions induced by the pump

beam, hence minimizing the overall amplitude of the temperature gradient within the sample. Therefore, we can use an alloy metal transducer to reduce the thermal conductivity of the metal transducer layer and maintain more of an in-plane temperature gradient within the sample. Here, we used an AJA International sputter to deposit a 2-nm Ti adhesion layer and co-sputtered a 70-nm Au_{0.93}Ti_{0.07} alloy layer. The sheet resistance was $18.04 \pm 0.36 \Omega/\text{sq}$, corresponding to an electronic thermal conductivity of $5.4 \text{ W m}^{-1} \text{ K}^{-1}$. The actual thermal conductivity was found to be $6.5 \text{ W m}^{-1} \text{ K}^{-1}$ by fitting three reference samples across all temperatures. The small difference between the thermal conductivity used in fitting and the value from four-point probe measurements is attributed partly to phonon contributions and partly to the anisotropic thermal conductivity. The latter might arise from the columnar grain boundaries affecting in-plane electron transport. In Fig. S11 to Fig. S13, we show benchmark measurements using the alloy transducer to confirm the accuracy of the corresponding FDTR results. In Fig. S14, we present the corresponding FDTR data for the alloy-coated sample, which validates our measurements on Fe[HB(tz)₃]₂ using the gold transducer layer as presented in the main text.

Sensitivity and uncertainty analysis

The nonlinear least-square optimization method was used for FDTR data fitting. In the least-square nonlinear optimization, the fitting residual is a vector function of dimension N_ω (number of modulation frequency points) given by $\mathbf{f}(\mathbf{X}) = \boldsymbol{\phi}_{\text{exp}} - \boldsymbol{\phi}_{\text{model}}(\mathbf{X})$, where $\mathbf{X} = (x_1, x_2, \dots, x_p)$ is the vector consisting of p variables to be fitted, $\boldsymbol{\phi}_{\text{model}}(\mathbf{X})$ is the phase lag calculated using the Fourier heat diffusion model, and $\boldsymbol{\phi}_{\text{exp}} = (\theta_{F_1}, \theta_{F_2}, \dots, \theta_{F_N})$ is the experimental phase lag at N modulation frequencies, F_1, F_2, \dots, F_N , measured by FDTR. The sensitivity vector to the fitting variable x_i can be computed by $\frac{\partial \boldsymbol{\phi}_{\text{model}}}{\partial x_i}$. The magnitude of the sensitivity vector indicates how sensitive the fitting variable x_i is in the fitting problem.

The sum of squared residuals is the objective function to be minimized, expressed as $R(\mathbf{X}) = \sum_{i=1}^{N_\omega} f_i(\mathbf{X})^2$. Consider fitting two variables κ and G as an example, where $\mathbf{X} = (\kappa, G)$. Ideally, at the best fit $\mathbf{X}_0 = (\kappa_0, G_0)$, the sum of residuals is small such that $R(\kappa_0, G_0) \approx 0$ (in an actual experiment, $R(\kappa_0, G_0)$ is a finite quantity due to inevitable noise). In the parameter space near the optimal fit \mathbf{X}_0 , we can make the following approximation:

$$R(\kappa, G) \approx \left| \left(\frac{\partial \boldsymbol{\phi}_{\text{model}}}{\partial \kappa} \right) \Big|_{\mathbf{X}_0} \right|^2 (\kappa - \kappa_0)^2 + \left| \left(\frac{\partial \boldsymbol{\phi}_{\text{model}}}{\partial G} \right) \Big|_{\mathbf{X}_0} \right|^2 (G - G_0)^2, \quad \text{Eq. S1}$$

where $\left| \frac{\partial \boldsymbol{\phi}_{\text{model}}}{\partial x_i} \Big|_{\mathbf{X}_0} \right|^2 = \sum_{i=1}^{N_\omega} \left(\frac{\partial \phi_{\text{model},i}}{\partial \kappa} \Big|_{\mathbf{X}_0} \right)^2$ is the sum of squared elements in the sensitivity vector.

In other words, the second derivative of $R(\mathbf{X})$ near the best fit is twice the squared magnitude of the sensitivity vector. If there is a large curvature along a certain axis, the sensitivity to the fitting variable associated with that axis is high. Therefore, examining the local curvature near the minimum of an $R(\mathbf{X})$ map provides information about the sensitivity of the fitting to different variables.

We performed an uncertainty analysis to determine whether certain fitting variables are correlated and to evaluate the confidence level in the data fitting. In the uncertainty analysis, the Mahalanobis

distance is introduced, defined by $D = (\mathbf{X} - \boldsymbol{\mu})^T \boldsymbol{\Sigma}^{-1} (\mathbf{X} - \boldsymbol{\mu})$, where $\boldsymbol{\mu}$ is the expected value of \mathbf{X} and $\boldsymbol{\Sigma}$ is the variance-covariance matrix. The detailed procedures to compute $\boldsymbol{\Sigma}$ can be found in Ref.⁴⁷. The Mahalanobis distance is a dimensionless quantity that measures the distance from the sample data to the expected value. We use the isosurface of the Mahalanobis distance to represent the confidence interval:

$$\Pr(D \leq \chi_{p,\alpha}^2) = \alpha, \quad \text{Eq. S2}$$

where \Pr stands for probability, α is the confidence level, and $\chi_{p,\alpha}^2$ is the chi-squared distribution with degree of freedom p . Note that the degree of freedom p is the same as the size of the vector \mathbf{X} . When $p = 2$ and $\alpha = 0.63$, we have $\chi_{p,\alpha}^2 = 2$. If x_1 and x_2 of \mathbf{X} are completely independent variables with standard deviations σ_1 and σ_2 , the Mahalanobis distance is reduced to $D = \frac{(x_1 - \mu_1)^2}{\sigma_1^2} + \frac{(x_2 - \mu_2)^2}{\sigma_2^2}$, which describes an ellipsoid whose principal axes lie on the x- and y- axes. Therefore, the confidence interval $\Pr(D \leq 2) = 0.63$ corresponds to the region within “ 1σ ” distance to the expected value.

In Fig. S10a, we observe that the FDTR signal for the LS phase is most sensitive to the cross-plane thermal conductivity κ_z , the thermal boundary conductance G , the effective beam radius r_{eff} , and the heat capacity C . The latter two quantities can be measured separately (from beam offset measurements and PPMS measurements, respectively). Therefore, we choose κ_z and G as fitting variables. The sensitivity to G of the HS phase becomes lower than that of the LS phase, yet the sensitivity to κ_z remains high (Fig. S10b). Figs. S10c and S10d show that κ_z and G are mildly anti-correlated in the LS phase and anti-correlated in the HS phase, which still allows us to determine the best fit for κ_z , despite a slightly elevated uncertainty in κ_z of the LS phase and a high uncertainty in G of the HS phase.

Modeling thermal transport in materials under modulated laser heating

Thermal transport in solid materials has been previously studied using pump-probe spectroscopy methods^{51–53}, and here we outline how to use Fourier’s law of heat conduction to model the FDTR signal. The heat equation under laser heating is,

$$\rho c \frac{\partial T}{\partial t} = \nabla \cdot (\boldsymbol{\kappa} \cdot \nabla T) + P, \quad \text{Eq. S3}$$

where $\boldsymbol{\kappa} = \begin{pmatrix} \kappa_{xx} & \kappa_{xy} & \kappa_{xz} \\ \kappa_{yx} & \kappa_{yy} & \kappa_{yz} \\ \kappa_{zx} & \kappa_{zy} & \kappa_{zz} \end{pmatrix}$ is the thermal conductivity tensor, c is the gravimetric specific heat,

ρ is the mass density, and $P = \frac{2P_0}{\pi\sigma_x\sigma_y} e^{-2x^2/\sigma_x^2} e^{-2y^2/\sigma_y^2} e^{-\alpha z} e^{i\omega t}$ is the heating power density with P_0 being the amplitude of the absorbed pump power. Here, σ_x and σ_y are $1/e^2$ pump beam radii in the x- and y-directions, α is the inverse penetration depth for the pump laser beam, and $\omega = 2\pi f$ where f is the modulation frequency. Specifically, the heat flux along the z-axis (normal to the sample surface) is given by $q_z = -\left(\kappa_{zx} \frac{\partial T}{\partial x} + \kappa_{zy} \frac{\partial T}{\partial y} + \kappa_{zz} \frac{\partial T}{\partial z}\right)$. We apply the Fourier transform to the heat equation in the in-plane directions,

$$\frac{\partial^2 \tilde{T}}{\partial z^2} + \lambda_1 \frac{\partial \tilde{T}}{\partial z} - \lambda_0 \tilde{T} + \frac{\tilde{P}}{\kappa_{zz}} = 0, \quad \text{Eq. S4}$$

where $\lambda_1 = 2i \left(\frac{\kappa_{xz}}{\kappa_{zz}} q_x + \frac{\kappa_{yz}}{\kappa_{zz}} q_y \right)$, $\lambda_0 = i \frac{\rho c \omega}{\kappa_{zz}} + \frac{\kappa_{xx}}{\kappa_{zz}} q_x^2 + \frac{\kappa_{yy}}{\kappa_{zz}} q_y^2 + \frac{\kappa_{xy}}{\kappa_{zz}} q_x q_y$, and $\tilde{P} = P_0 e^{-\sigma_x^2 q_x^2/8} e^{-\sigma_y^2 q_y^2/8} \alpha e^{-\alpha z}$. The solution to the above equation takes the form,

$$\tilde{T} = C e^{\alpha z} + D e^{b z} + F e^{-\alpha z}, \quad \text{Eq. S5}$$

where $a = \frac{-\lambda_1 + \sqrt{\lambda_1^2 + 4\lambda_0}}{2}$, $b = \frac{-\lambda_1 - \sqrt{\lambda_1^2 + 4\lambda_0}}{2}$ and $F = \frac{1}{\kappa_{zz}} \frac{P_0 \alpha}{\lambda_0 + \lambda_1 \alpha - \alpha^2} e^{-\sigma_x^2 q_x^2/8} e^{-\sigma_y^2 q_y^2/8}$. Note that here \tilde{T} represents the temperature deviation from the background temperature (i.e., the temperature indicated by thermocouple readings) rather than the absolute temperature. In the following, we will simply use the term temperature to describe the temperature deviation from background temperature for conciseness. The temperature and the heat flux at the bottom of the first layer, i.e., the metal transducer layer, can be expressed by,

$$\begin{pmatrix} \tilde{T}(z=L) \\ \tilde{q}_z(z=L) \end{pmatrix} = \mathbf{M}_1 \begin{pmatrix} \tilde{T}(z=0) \\ F \end{pmatrix}, \quad \text{Eq. S6}$$

$$\mathbf{M}_1 = \frac{e^{\alpha L}}{\gamma_a - \gamma_b} \begin{pmatrix} -\gamma_b + \gamma_a e^{(b-a)L} & -(\gamma_c - \gamma_b) + (\gamma_c - \gamma_a) e^{(b-a)L} + (\gamma_a - \gamma_b) e^{-(\alpha+a)L} \\ \gamma_a \gamma_b (1 - e^{(b-a)L}) & (\gamma_c - \gamma_b) \gamma_a - (\gamma_c - \gamma_a) \gamma_b e^{(b-a)L} - (\gamma_a - \gamma_b) \gamma_c e^{-(\alpha+a)L} \end{pmatrix} \quad \text{Eq. S7}$$

where $\gamma_a = \kappa_{zz} a + i q_x \kappa_{zx} + i q_y \kappa_{zy}$, $\gamma_b = \kappa_{zz} b + i q_x \kappa_{zx} + i q_y \kappa_{zy}$, $\gamma_c = -\kappa_{zz} \alpha + i q_x \kappa_{zx} + i q_y \kappa_{zy}$, and L is the thickness of the first layer. The temperature and heat flux at the interface between the first and the second layer satisfy,

$$\begin{pmatrix} \tilde{T}'(z=0) \\ \tilde{q}_z'(z=0) \end{pmatrix} = \mathbf{M}_2 \begin{pmatrix} \tilde{T}(z=L) \\ \tilde{q}_z(z=L) \end{pmatrix}, \quad \text{Eq. S8}$$

where $\mathbf{M}_2 = \begin{pmatrix} 1 & -\frac{1}{G} \\ 0 & 1 \end{pmatrix}$ and G is the interfacial thermal conductance. The temperature and heat flux at the bottom of the second layer can be expressed by,

$$\begin{pmatrix} \tilde{T}'(z=L') \\ \tilde{q}_z'(z=L') \end{pmatrix} = \mathbf{M}_3 \begin{pmatrix} \tilde{T}'(z=0) \\ \tilde{q}_z'(z=0) \end{pmatrix}, \quad \text{Eq. S9}$$

$$\mathbf{M}_3 = \frac{e^{a'L'}}{\gamma'_a - \gamma'_b} \begin{pmatrix} -\gamma'_b + \gamma'_a e^{(b'-a')L'} & -1 + e^{(b'-a')L'} \\ \gamma'_a \gamma'_b (1 - e^{(b'-a')L'}) & \gamma'_a - \gamma'_b e^{(b'-a')L'} \end{pmatrix}, \quad \text{Eq. S10}$$

where L' is the thickness of the second layer. As a consequence, we arrive at the following relation,

$$\begin{pmatrix} \tilde{T}'(z = L') \\ \tilde{q}_z'(z = L') \end{pmatrix} = \mathbf{M} \begin{pmatrix} \tilde{T}(z = 0) \\ F \end{pmatrix}, \quad \text{Eq. S11}$$

where $\mathbf{M} = \mathbf{M}_3 \mathbf{M}_2 \mathbf{M}_1$. We further consider the adiabatic boundary conditions $\tilde{q}_z'(z = L') = 0$ and $\tilde{q}_z(z = 0) = 0$ and obtain that,

$$\tilde{T}(z = 0) = -\frac{M_{22}}{M_{21}} F, \quad \text{Eq. S12}$$

where M_{22} and M_{21} are the matrix elements of \mathbf{M} . Here, for simplicity, we only discussed the case of two layers, but one can easily extend this formalism to the case of any number of layers.

The surface temperature profile can be computed by taking the inverse Fourier transform,

$$T(x, y) = \frac{1}{(2\pi)^2} \iint dq_x dq_y \tilde{T}(z = 0) e^{iq_x x} e^{iq_y y}, \quad \text{Eq. S13}$$

As a result, the signal detected by the probe beam is,

$$\begin{aligned} I(\omega) &= \text{CTR} \iint dx dy \frac{2}{\pi \sigma'_x \sigma'_y} T(x, y) e^{-\frac{2(x-x_o)^2}{\sigma'^2_x}} e^{-\frac{2(y-y_o)^2}{\sigma'^2_y}} \\ &= \frac{\text{CTR}}{(2\pi)^2} \iint dq_x dq_y \frac{1}{\kappa_{zz}} \left(-\frac{M_{22}}{M_{21}} \right) \frac{P_0 \alpha}{\lambda_0 + \lambda_1 \alpha - \alpha^2} e^{-\frac{q_x^2 r_x^2}{4}} e^{-\frac{q_y^2 r_y^2}{4}} e^{-iq_x x_o} e^{-iq_y y_o}, \end{aligned} \quad \text{Eq. S14}$$

where CTR is the coefficient of thermoreflectance, κ_{zz} is the thermal conductivity of the metal transducer rather than that of the sample, σ'_x and σ'_y are the probe beam radii along the x- and y-directions, x_o and y_o are the beam offset distance of the probe beam center with respect to the pump beam center along the x- and y-directions, and $r_x = \sqrt{(\sigma_x^2 + \sigma'^2_x)/2}$ and $r_y = \sqrt{(\sigma_y^2 + \sigma'^2_y)/2}$ are the effective radii along the x- and y-directions. In our setup, the difference between effective radii along x- and y-directions is less than 3%, hence we assume an isotropic effective radius⁴⁶. It is worth noting that the signal is only determined by the effective beam radius rather than the individual values of the pump or probe beam's radius.

Effect of electron-phonon coupling in the modeling of FDTR signals

In FDTR measurements, the incident photons from the pump beam first excite nonequilibrium (hot) electrons and holes in the metal transducer. The energy of these carriers is then gradually transferred to the lattice through electron-phonon interactions, until the electrons and phonons eventually converge to a common temperature. At the interface between the metal and a semiconductor (or an insulator such as Fe[HB(tz)₃]₂), the energy carried by electrons and holes cannot be directly transmitted across the interface. Instead, hot carriers must first transfer their energy to phonons through electron-phonon coupling, and it is these phonons that can transfer heat across the interface to phonons on the other side. As a result, when the timescale of optical pump-probe measurements is short, or when the metal layer is too thin for electrons and phonons to fully

equilibrate, electron-phonon coupling must be explicitly considered in the modeling, rather than relying solely on a Fourier-based heat conduction model^{54,55}.

Here, we investigate the effect of nonequilibrium electron-phonon coupling in the gold transducer layer on the phase lag of FDTR using a two-temperature model⁵⁶, with the detailed implementation provided in our data repository. We solve for the spatial profiles of electron and phonon temperature deviations from the background. In particular, the thermoreflectance is dominated by the phonon temperature in gold⁵⁷. As shown in Fig. S16a and b, the difference between electron and phonon temperatures is pronounced for the Au/Si case, yet almost negligible for the Au/Fe[HB(tz)₃]₂ case at a modulation frequency of 10 MHz. This is because, at this modulation frequency, the thermal resistance associated with nonequilibrium electron-phonon coupling is significantly lower than the effective thermal resistance of Fe[HB(tz)₃]₂, yet comparable with that of Si. This behavior persists in the modulation frequency ranging from 10⁵ Hz to 5 × 10⁷ Hz. Over this range, the phase lags of the temperatures calculated using the two-temperature model and the Fourier-based heat conduction model differ noticeably for Si but not for Fe[HB(tz)₃]₂ (see Fig. S16c and d). Therefore, the Fourier heat conduction model alone is sufficient for modeling the measured phase lag for Fe[HB(tz)₃]₂.

Estimation of the temperature rise due to pump and probe heating

When the thermal penetration depth $\sqrt{\frac{2\kappa}{C\omega}}$ is much smaller than the effective beam radius r_{eff} , the measured thermoreflectance is determined by the effusivity⁵⁸. In this scenario, the amplitude of the sinusoidal temperature deviation is approximately given by, $\Delta T \approx \frac{P}{\pi r_{\text{eff}}^2 \sqrt{\omega \kappa C}}$, where P is the absorbed pump power, and $\sqrt{\kappa C}$ is the thermal effusivity. Note that the time-averaged temperature rise is also given by ΔT . For Fe[HB(tz)₃]₂ at 298 K in the LS phase, the thermal effusivity is 1.12 × 10³ J/(m² K s^{1/2}). In our measurements, we used a pump power of 1 mW and effective beam size of 3 μm. The absorptance of the gold transducer layer of 100 nm is 0.61 at 458 nm. Accordingly, we estimate that at $f = 1$ MHz, $\Delta T \approx 7.7$ K and at $f = 10$ MHz, $\Delta T \approx 2.4$ K. Therefore, we use a temperature window of ±5 K near the phase transition temperature in Fig. 1 to highlight the possible coexistence of two spin phases due to the pump laser heating. In the HS phase, the thermal effusivity decreases by roughly a factor of 2, and ΔT increase roughly by a factor of $\sqrt{2}$. For Fe(Fpr-trz₂-dmpn)(NCS)₂, the thermal effusivity is 628 J/(m² K s^{1/2}) in the LS phase and 360 J/(m² K s^{1/2}) in the HS phase near the SCO transition temperature. The average temperature rise ΔT in Fe(Fpr-trz₂-dmpn)(NCS)₂ is estimated to be 7 K and 13 K for the LS phase and HS phase, respectively. Similarly, we use a temperature window of ±7 K to highlight the possible coexistence of two spin phases in Fe(Fpr-trz₂-dmpn)(NCS)₂ near the SCO transition temperature in Fig. 5.

As for the probe laser, we used a probe power of 3 mW. The absorptance of the gold layer is around 0.22 at 532 nm. Therefore, the DC probe heating power is estimated to be 0.66 mW. For every FDTR measurement with a frequency sweep, it is essential to first balance the power of the reflected probe and the reference probe, which is achieved by rotating a half-wave plate to adjust the reference probe's power and takes approximately 5s. During this balancing process and the subsequent data acquisition process, the probe beam continuously heats the sample for 5 to 10s. During this time, with an estimated sample volume of 250 μm × 100 μm × 5 μm and a Si substrate volume of 5 mm × 5 mm × 1 mm, and with thermal diffusivities on the order of 0.1 mm²/s for the

sample and $0.8 \text{ cm}^2/\text{s}$ for the Si substrate, heat has already diffused throughout both the sample and the substrate, and significantly into the temperature stage.

Before the heat diffuses into the substrate, the sample's temperature keeps rising. Once heat diffuses into the substrate, it can be effectively dissipated, and the sample temperature is likely to increase minimally further. Therefore, we use the temperature at the moment heat begins to diffuse into the substrate to estimate the maximum sample temperature rise. Due to the gold transducer's thermal conductivity ($180 \text{ W m}^{-1} \text{ K}^{-1}$ at room temperature) being several hundred times greater than that of the sample, the heating applied to the sample surface can be approximated as uniform. The temperature profile within the sample is expressed by⁵⁹,

$$\Delta T(z, t) = \frac{P}{\kappa A} \left[2 \sqrt{\frac{\alpha t}{\pi}} \exp\left(-\frac{z^2}{4\alpha t}\right) - z \operatorname{erfc}\left(\frac{z}{2\sqrt{\alpha t}}\right) \right], \quad \text{Eq. S15}$$

where P is the absorbed probe power, A is the effective area (i.e., the surface area of the gold transducer), and $\alpha = \kappa/C$ is the thermal diffusivity of the sample. The temperature rise at the sample surface, when the diffusion length $\sqrt{\alpha t}$ is comparable to the sample thickness $t_{\text{thickness}}$, is given by $\Delta T(0, t_{\text{thickness}}^2/\alpha) = \frac{2Pt_{\text{thickness}}}{\sqrt{\pi\kappa A}} = 0.7 \text{ K}$ in the HS phase. The corresponding temperature rise in the LS phase is estimated to be only 0.2 K.

After the heat diffuses into the Si substrate, we can approximate the sample as a point heater due to the size contrast between the sample and the substrate. We also assume that the cryostat stage, made of Al, has the same thermal conductivity and thermal diffusivity as Si. Accordingly, the temperature profile within the substrate and temperature stage is given by⁶⁰,

$$\Delta T(r, t) = \frac{P}{4\pi\kappa_{\text{Si}} r} \operatorname{erfc}\left(\frac{r}{2\sqrt{\alpha_{\text{Si}} t}}\right), \quad \text{Eq. S16}$$

where r is the distance to the center of the sample's bottom surface. The average temperature rise within the diffusion length $\sqrt{\alpha_{\text{Si}} t}$ scales with time as $\bar{\Delta T} \propto \frac{P}{\kappa_{\text{Si}} \sqrt{\alpha_{\text{Si}} t}}$, showing a decrease over time.

Plugging in $t = 10 \text{ s}$, we find only a small average temperature rise, $\bar{\Delta T} \propto 3 \times 10^{-4} \text{ K}$. This supports our argument that the substrate and the temperature stage can effectively dissipate heat once it arrives. Hence, Eq. S15 serves as an effective measure of the peak sample temperature rise due to probe laser heating. From the above analysis, we also recognize that using a high-thermal-conductivity substrate, using silver paste to adhere the sample to the cryostat, applying a low probe laser power, and choosing a sample with a large area and a small thickness are necessary to reduce the temperature rise.

However, when using an alloy transducer with a thermal conductivity of $5.4 \text{ W m}^{-1} \text{ K}^{-1}$, the uniform heating assumption in Eq. S15 is no longer valid. Instead, the effective area A can be reduced by a factor of more than 30. In addition, the required probe laser power is 1.6 times higher. Collectively, the temperature rise in the sample can exceed 30 K, indicating that probe-induced temperature rise cannot be neglected when using an alloy transducer.

Analysis of the powder neutron scattering data

We start with the elastic part of powder neutron scattering. For neutron scattering in a single crystal, the coherent elastic neutron cross section is³⁶,

$$\left(\frac{d\sigma}{d\Omega}\right)_{coh} = N \frac{(2\pi)^3}{V} e^{-2W(\mathbf{Q})} \sum_{\mathbf{G}} |S_{\mathbf{G}}|^2 \delta(\mathbf{Q} - \mathbf{G}), \quad \text{Eq. S17}$$

where N is the number of unit cells, V is the unit cell volume, $S_{\mathbf{G}} = \sum_{\mathbf{d}} b_{\mathbf{d}} e^{i\mathbf{G}\cdot\mathbf{d}}$ is the structure factor, $b_{\mathbf{d}}$ is the neutron scattering length for the atom at position \mathbf{d} , \mathbf{G} is the reciprocal lattice vector, and $W(\mathbf{Q})$ is the Debye-Waller factor, which is close to 1 at the temperatures of interest. The intensity of Bragg scattering is,

$$I(\theta) = m_{hkl} |S_{hkl}|^2 L(\theta) \exp\left(-4 \ln 2 \left(\frac{2\theta - 2\theta_{hkl}}{\Gamma}\right)^2\right), \quad \text{Eq. S18}$$

where m_{hkl} is the multiplicity of the Bragg reflection (h, k, l) and $L(\theta) = 1/\sin(\theta)\sin(2\theta)$ is the Lorentz factor. In a polycrystalline sample, we sum over Bragg scattering intensities for all combinations of h, k, l to obtain the total elastic scattering intensity (Fig. S18).

Strässle *et al.* derived an explicit expression for the inelastic neutron scattering cross section in materials with a single-atom unit cell³⁶. In the following, we generalize this derivation to materials with a multi-atom unit cell.

The position of an atom in the lattice can be expressed by,

$$\mathbf{r}_{\tau j}(t) = \mathbf{R}_{\tau} + \mathbf{d}_j + \mathbf{u}_j(\mathbf{R}_{\tau}, t), \quad \text{Eq. S19}$$

where \mathbf{R}_{τ} is the position of the τ th unit cell in the Bravais lattice, \mathbf{d}_j is the equilibrium position of the j th atom within the unit cell relative to the lattice site, and $\mathbf{u}_j(\mathbf{R}_{\tau}, t)$ is the atomic displacement. The atomic displacement operator can be written as,

$$\hat{\mathbf{u}}_j(\mathbf{R}_{\tau}, t) = \sqrt{\frac{\hbar}{2N_{uc}}} \sum_{qv} \frac{\mathbf{e}_{vj}(\mathbf{q})}{\sqrt{M_j \omega_v(\mathbf{q})}} (\hat{a}_v(\mathbf{q}) e^{i[\mathbf{q}\cdot\mathbf{R}_{\tau} - \omega_v(\mathbf{q})t]} + \hat{a}_v^\dagger(\mathbf{q}) e^{-i[\mathbf{q}\cdot\mathbf{R}_{\tau} - \omega_v(\mathbf{q})t]}), \quad \text{Eq. S20}$$

where \mathbf{q} is the phonon wavevector defined in the first Brillouin zone, N_{uc} is the number of unit cells, M_j is the mass, $\mathbf{e}_{vj}(\mathbf{q})$ is the phonon eigenvector, and $\omega_v(\mathbf{q})$ is the phonon frequency of branch v . Here, the phonon creation and annihilation operators, $\hat{a}_v^\dagger(\mathbf{q})$ and $\hat{a}_v(\mathbf{q})$, satisfy the following relations,

$$[\hat{a}_v(\mathbf{q}), \hat{a}_{v'}^\dagger(\mathbf{q}')] = \delta_{vv'} \delta_{\mathbf{q}\mathbf{q}'}, \quad \text{Eq. S21}$$

$$[\hat{a}_v(\mathbf{q}), \hat{a}_{v'}(\mathbf{q}') = 0, \quad \text{Eq. S22}$$

$$[\hat{a}_\nu^\dagger(\mathbf{q}), \hat{a}_{\nu'}^\dagger(\mathbf{q}')]=0. \quad \text{Eq. S23}$$

For neutrons scattered by atoms, the scattering cross section is given by,

$$\begin{aligned} \frac{d^2\sigma}{d\Omega d\omega} &= \frac{1}{2\pi\hbar} \frac{k'}{k} \sum_{\mathbf{R}_\tau, \mathbf{R}_{\tau'}, \mathbf{d}_j, \mathbf{d}_{j'}} b_{j'}(\mathbf{R}_{\tau'}) b_j(\mathbf{R}_\tau) e^{i\mathbf{Q}\cdot(\mathbf{R}_\tau + \mathbf{d}_j - \mathbf{R}_{\tau'} - \mathbf{d}_{j'})} \\ &\times \int_{-\infty}^{+\infty} \langle e^{-i\mathbf{Q}\cdot\mathbf{u}_{j'}(\mathbf{R}_{\tau'}, 0)} e^{i\mathbf{Q}\cdot\mathbf{u}_j(\mathbf{R}_\tau, t)} \rangle e^{-i\omega t} dt, \end{aligned} \quad \text{Eq. S24}$$

where $b_j(\mathbf{R}_\tau)$ is the neutron scattering length, and k and k' are the wavevectors of the incoming and outgoing neutrons, respectively. The momentum transfer \mathbf{Q} is defined as $\mathbf{Q} = \mathbf{k} - \mathbf{k}'$. The angle bracket denotes the expectation value of the operator within, which is calculated as $\langle \hat{O} \rangle = \sum_\lambda p_\lambda \langle \lambda | \hat{O} | \lambda \rangle$, with \hat{O} being the operator, p_λ the probability of the scatter (the atom) in state $|\lambda\rangle$, and $|\lambda\rangle$ the wavefunction. Denote the exponents in Eq. S24 as follows,

$$\hat{A} = -i\mathbf{Q} \cdot \mathbf{u}_{j'}(\mathbf{R}_{\tau'}, 0) = -i \sum_{\mathbf{q}\nu} \left(\alpha_{\nu j'}(\mathbf{q}) \hat{a}_\nu(\mathbf{q}) + \alpha_{\nu j'}^*(\mathbf{q}) \hat{a}_\nu^\dagger(\mathbf{q}) \right), \quad \text{Eq. S25}$$

$$\hat{B} = i\mathbf{Q} \cdot \mathbf{u}_j(\mathbf{R}_\tau, t) = i \sum_{\mathbf{q}\nu} \left(\beta_{\nu j}(\mathbf{q}) \hat{a}_\nu(\mathbf{q}) + \beta_{\nu j}^*(\mathbf{q}) \hat{a}_\nu^\dagger(\mathbf{q}) \right), \quad \text{Eq. S26}$$

where the coefficients $\alpha_{\nu j'}(\mathbf{q})$ and $\beta_{\nu j}(\mathbf{q})$ are specified by,

$$\alpha_{\nu j'}(\mathbf{q}) = \sqrt{\frac{\hbar}{2N_{uc}}} \frac{\mathbf{Q} \cdot \mathbf{e}_{\nu j'}(\mathbf{q})}{\sqrt{M_{j'} \omega_\nu(\mathbf{q})}} e^{i\mathbf{q}\cdot\mathbf{R}_{\tau'}}, \quad \text{Eq. S27}$$

$$\beta_{\nu j}(\mathbf{q}) = \sqrt{\frac{\hbar}{2N_{uc}}} \frac{\mathbf{Q} \cdot \mathbf{e}_{\nu j}(\mathbf{q})}{\sqrt{M_j \omega_\nu(\mathbf{q})}} e^{i[\mathbf{q}\cdot\mathbf{R}_\tau - \omega_\nu(\mathbf{q})t]}. \quad \text{Eq. S28}$$

The exponential term in Eq. S24 can be expanded using the following identity,

$$\langle e^{\hat{A}} e^{\hat{B}} \rangle = e^{-2W_j(\mathbf{Q})} e^{\langle \hat{A} \hat{B} \rangle} = e^{-2W_j(\mathbf{Q})} \left[1 + \langle \hat{A} \hat{B} \rangle + \frac{1}{2} \langle \hat{A} \hat{B} \rangle^2 + \dots \right], \quad \text{Eq. S29}$$

where the term $e^{-2W_j(\mathbf{Q})}$ is the Debye–Waller factor for the j th atom and the first term in the Taylor series corresponds to elastic neutron scattering. On the other hand, the second term, as the leading contribution in the remainder of the series, determines the inelastic neutron scattering cross section. Furthermore, when summing over all possible atom pairs, $\sum_{\mathbf{R}_\tau, \mathbf{R}_{\tau'}, \mathbf{d}_j, \mathbf{d}_{j'}} \dots$, the terms can be divided into two groups: those where τj and $\tau' j'$ refer to different atoms, and those where τj and $\tau' j'$ refer to the same atom. Specifically, for the first group where the neutron scattering lengths of the two atoms are independent, the following identity holds,

$$\sum_{\substack{\mathbf{R}_\tau, \mathbf{R}_{\tau'}, \\ \mathbf{d}_j, \mathbf{d}_{j'}}} b_{j'}(\mathbf{R}_{\tau'}) b_j(\mathbf{R}_\tau) e^{i\mathbf{Q}\cdot(\mathbf{R}_\tau + \mathbf{d}_j - \mathbf{R}_{\tau'} - \mathbf{d}_{j'})} \dots = N_{uc} \sum_{\mathbf{L}, \mathbf{d}_j, \mathbf{d}_{j'}} \langle b_j \rangle^2 e^{i\mathbf{Q}\cdot(\mathbf{d}_j - \mathbf{d}_{j'})} e^{i\mathbf{Q}\cdot\mathbf{L}} \dots, \quad \text{Eq. S30}$$

where $\langle b_j \rangle$ is the neutron scattering length averaged over the sample volume and $\mathbf{L} = \mathbf{R}_\tau - \mathbf{R}_{\tau'}$. The first group accounts for the coherent inelastic neutron scattering, whose cross section is expressed as,

$$\frac{d^2\sigma_{coh}}{d\Omega d\omega} = \frac{1}{2} \frac{k'}{k} \sum_{qv} \frac{1}{\omega_v(\mathbf{q})} \left| \sum_j \langle b_j \rangle \frac{\mathbf{Q} \cdot \mathbf{e}_{vj}(\mathbf{q})}{\sqrt{M_j}} e^{-W_j(\mathbf{Q})} e^{i\mathbf{Q}\cdot\mathbf{d}_j} \right|^2 \times \begin{bmatrix} (n_v(\mathbf{q}) + 1) \delta(\omega - \omega_v(\mathbf{q})) \sum_{\mathbf{G}} \frac{(2\pi)^3}{V} \delta(\mathbf{Q} - \mathbf{q} - \mathbf{G}) \\ + n_v(\mathbf{q}) \delta(\omega + \omega_v(\mathbf{q})) \sum_{\mathbf{G}} \frac{(2\pi)^3}{V} \delta(\mathbf{Q} + \mathbf{q} - \mathbf{G}) \end{bmatrix}, \quad \text{Eq. S31}$$

where V is the unit-cell volume. Note that Eq. S31 also includes the case where the two atoms are the same, but their scattering lengths are temporally uncorrelated.

The second group accounts for the incoherent inelastic neutron scattering and the corresponding cross section is given as,

$$\frac{d^2\sigma_{inc}}{d\Omega d\omega} = \frac{1}{2} \frac{k'}{k} \sum_{qv} \frac{1}{\omega_v(\mathbf{q})} \left[\sum_j (\langle b_j^2 \rangle - \langle b_j \rangle^2) \frac{|\mathbf{Q} \cdot \mathbf{e}_{vj}(\mathbf{q})|^2}{M_j} e^{-2W_j(\mathbf{Q})} \right] \times [(n_v(\mathbf{q}) + 1) \delta(\omega - \omega_v(\mathbf{q})) + n_v(\mathbf{q}) \delta(\omega + \omega_v(\mathbf{q}))] \quad \text{Eq. S32}$$

where $\langle b_j^2 \rangle$ is the expectation value of the squared neutron scattering length for the j th atom. Note that the coherent contribution, which has already been accounted for in Eq. S31, has been subtracted.

For a powder sample with sufficient crystal orientation diversity, the ensemble average yields the following identity:

$$\langle |\mathbf{Q} \cdot \mathbf{e}_{vj}(\mathbf{q})|^2 \rangle = \langle \cos^2 \theta \rangle Q^2 |\mathbf{e}_{vj}(\mathbf{q})|^2 = \frac{1}{3} Q^2 |\mathbf{e}_{vj}(\mathbf{q})|^2. \quad \text{Eq. S33}$$

Resultantly, the incoherent inelastic neutron scattering cross section on the energy gain side can be written as,

$$\begin{aligned}
\frac{d^2\sigma_{\text{inc}}}{d\Omega d\omega} &= \frac{1}{6} \frac{k'}{k} \frac{(n(\omega) + 1)Q^2}{\omega} \left[\sum_j (\langle b_j^2 \rangle - \langle b_j \rangle^2) \frac{1}{M_j} e^{-2W_j(Q)} \sum_{qv} |\mathbf{e}_{vj}(\mathbf{q})|^2 \delta(\omega - \omega_v(\mathbf{q})) \right] \\
&= \frac{1}{6} \frac{k'}{k} \frac{(n(\omega) + 1)Q^2}{\omega} \left[\sum_j (\langle b_j^2 \rangle - \langle b_j \rangle^2) \frac{1}{M_j} e^{-2W_j(Q)} g_j(\omega) \right] \\
&= \frac{1}{6} \frac{k'}{k} \frac{(n(\omega) + 1)Q^2}{\omega} \text{GDOS}(\omega),
\end{aligned}$$

Eq. S34

where $g_j(\omega) = \sum_{qv} |\mathbf{e}_{vj}(\mathbf{q})|^2 \delta(\omega - \omega_v(\mathbf{q}))$ is the formal expression for the partial phonon density of states for atom j , and $\text{GDOS}(\omega) = \sum_j (\langle b_j^2 \rangle - \langle b_j \rangle^2) \frac{1}{M_j} e^{-2W_j(Q)} g_j(\omega)$ is the generalized phonon density of states, defined as the weighted sum of the partial phonon densities of states. Crucially, Eq. S34 establishes the relationship between the generalized phonon density of states and the incoherent inelastic neutron scattering cross section.

In measuring $\text{Fe}[\text{HB}(\text{tz})_3]_2$, the intensity of incoherent inelastic scattering is significantly stronger than that of coherent inelastic scattering due to the ubiquitous presence of hydrogen atoms, whose incoherent cross section ($\sigma_{\text{inc}} = 4\pi\langle b_{\text{H}}^2 \rangle - \langle b_{\text{H}} \rangle^2$) is much larger than its coherent cross section ($\sigma_{\text{coh}} = 4\pi\langle b_{\text{H}} \rangle^2$), as well as the incoherent and coherent cross sections of any other element. Moreover, the small mass of hydrogen atoms further amplifies their dominance in the total inelastic scattering cross section. As a result, the inelastic neutron scattering cross section on the energy gain side for our sample can be approximated by,

$$\begin{aligned}
\frac{d^2\sigma}{d\Omega d\omega} &\approx \frac{1}{6} \frac{k'}{k} (\langle b_{\text{H}}^2 \rangle - \langle b_{\text{H}} \rangle^2) e^{-2W_{\text{H}}(Q)} \frac{(n(\omega) + 1)Q^2}{M_{\text{H}}\omega} \sum_{qv} \sum_{j \in \text{H}} \delta(\omega - \omega_v(\mathbf{q})) |\mathbf{e}_{vj}(\mathbf{q})|^2 \\
&= \frac{1}{6} \frac{k'}{k} (\langle b_{\text{H}}^2 \rangle - \langle b_{\text{H}} \rangle^2) e^{-2W_{\text{H}}(Q)} \frac{(n(\omega) + 1)Q^2}{M_{\text{H}}\omega} g_{\text{H}}(\omega),
\end{aligned}$$

where M_{H} is the mass of a hydrogen atom, and $g_{\text{H}}(\omega)$ is the partial phonon density of states for hydrogen, i.e., the hydrogen-projected phonon density of states. The neutron momenta, k and k' , differ only minimally when the energy transfer is on the order of a typical phonon energy (in the THz range). If we further neglect the Debye–Waller factor $e^{-2W_{\text{H}}(Q)}$, an approximation that is generally acceptable except at high temperatures, we obtain the following relation:

$$g_{\text{H}}(\omega) \propto \frac{d^2\sigma}{d\Omega d\omega} \frac{\omega}{(n(\omega) + 1)Q^2}. \quad \text{Eq. S36}$$

Ideally, $g_{\text{H}}(\omega)$ can be obtained at a single, arbitrary Q . However, in practice, for the identity in Eq. S33 to hold, a full ensemble average over sufficiently diverse orientations is required, and varying Q effectively probes the sample from different orientations. Therefore, we perform an average of the expression in Eq. S36 over as wide a Q range as possible,

$$g_H(\omega) \propto \int \frac{d^2\sigma}{d\Omega d\omega} \frac{\omega}{(n(\omega) + 1)Q^2} dQ. \quad \text{Eq. S37}$$

Our DFTB calculations further show that the total phonon density of states $g(\omega)$ exhibits a similar pattern to the hydrogen-projected phonon density of states $g_H(\omega)$ (see Fig. S30), again because of the ubiquitous presence of hydrogen atoms in the lattice. This similarity allows us to use $g_H(\omega)$ as a proxy for the lattice dynamics of the entire material.

Weighted three-phonon scattering phase space

We aim to develop a metric to evaluate the phase space that accounts for three-phonon scattering processes that fulfill the energy conservation criterion. The three-phonon scattering rate is given by⁶¹,

$$\frac{1}{\tau} = \sum_{\lambda_1 \lambda_2} \left[W_{\lambda \lambda_1 \lambda_2}^+ + \frac{1}{2} W_{\lambda \lambda_1 \lambda_2}^- \right], \quad \text{Eq. S38}$$

Here, the three-phonon scattering probabilities, W , corresponding to the phonon absorption and phonon emission processes are defined by,

$$W_{\lambda \lambda_1 \lambda_2}^+ = \frac{2\pi}{\hbar} |\Phi_{\lambda \lambda_1 (-\lambda_2)}|^2 (f_{\lambda_1} - f_{\lambda_2}) \delta(\omega_\lambda + \omega_{\lambda_1} - \omega_{\lambda_2}), \quad \text{Eq. S39}$$

$$W_{\lambda \lambda_1 \lambda_2}^- = \frac{2\pi}{\hbar} |\Phi_{\lambda (-\lambda_1) (-\lambda_2)}|^2 (f_{\lambda_1} + f_{\lambda_2} + 1) \delta(\omega_\lambda - \omega_{\lambda_1} - \omega_{\lambda_2}), \quad \text{Eq. S40}$$

where λ denotes a phonon mode, f_λ is the Bose-Einstein distribution, and $\Phi_{\lambda \lambda_1 \lambda_2}$ is the three-phonon scattering matrix element. We can define the weighted three-phonon scattering phase space under the assumption that the wave-vector dependence of the scattering matrix is minimal,

$$P_\lambda = \sum_{\lambda_1 \lambda_2} \left[(f_{\lambda_1} - f_{\lambda_2}) \delta(\omega_\lambda + \omega_{\lambda_1} - \omega_{\lambda_2}) + \frac{1}{2} (f_{\lambda_1} + f_{\lambda_2} + 1) \delta(\omega_\lambda - \omega_{\lambda_1} - \omega_{\lambda_2}) \right]. \quad \text{Eq. S41}$$

This quantity measures the number of possible three-phonon scattering processes that conserve energy. By converting the summation into an integral, we obtain the following expression for the weighted three-phonon scattering phase space,

$$P(\omega) = V^2 \iint \left[(f(\omega_1) - f(\omega_2)) \delta(\omega + \omega_1 - \omega_2) + \frac{1}{2} (f(\omega_1) + f(\omega_2) + 1) \delta(\omega - \omega_1 - \omega_2) \right] g(\omega_1) g(\omega_2) d\omega_1 d\omega_2, \quad \text{Eq. S42}$$

where V is the volume of the unit cell and $g(\omega)$ is the phonon density of states. In numerical implementation, we use a Gaussian function with a standard deviation of 0.025 THz to represent the delta function.

Differentiating contributions of intramolecular and intermolecular interactions to phonon modes

In a molecular crystal, phonon modes involve both intramolecular and intermolecular interactions. Since the SCO transition significantly changes the intramolecular bonding strength while having a lesser effect on intermolecular bonding, it is important to quantify the relative contributions of intramolecular bonds and intermolecular bonds to specific phonon modes.

Here, we define a dimensionless quantity based on the Hessian (also known as the harmonic force constant) and phonon eigenvectors. The Hessian is defined as, $H_{ij}^{\alpha\beta} = \partial^2 E / \partial R_i^\alpha \partial R_j^\beta$, where E is the total energy and R_i^α is the Cartesian coordinate of the i -th atom along the α -axis. The dynamical matrix element at the zone center, i.e., the Γ point, is given by, $D_{ij}^{\alpha\beta} = H_{ij}^{\alpha\beta} / \sqrt{m_i m_j}$, where m_i is the mass of the i -th atom. The phonon frequency ω can be obtained by solving the eigenvalue problem, $\mathbf{D}\mathbf{u}_\lambda = \omega_\lambda^2 \mathbf{u}_\lambda$, where \mathbf{D} is the dynamical matrix and \mathbf{u}_λ is λ -th the phonon eigenvector. The dynamical matrix can be conveniently expressed as, $\mathbf{D} = \mathbf{M}\mathbf{H}\mathbf{M}$, where \mathbf{H} is the Hessian and \mathbf{M} is a diagonal matrix given by $M_{ij}^{\alpha\beta} = \frac{\delta_{ij}}{\sqrt{m_i}}$. Additionally, the phonon eigenvector is related to the atomic displacement via, $u_{\lambda i}^\alpha = \sqrt{m_i} U_{\lambda i}^\alpha$. Consequently, the Hamiltonian can be written as,

$$\begin{aligned} H &= \sum_{\lambda i \alpha} \left[\frac{\Pi_{\lambda i}^{\alpha*}(t) \Pi_{\lambda i}^\alpha(t)}{2m_i} + \frac{1}{2} \sum_{j \beta} U_{\lambda i}^{\alpha*}(t) H_{ij}^{\alpha\beta} U_{\lambda j}^\alpha(t) \right] \\ &= \sum_{\lambda i \alpha} \left[\frac{\Pi_{\lambda i}^{\alpha*}(t) \Pi_{\lambda i}^\alpha(t)}{2m_i} + \frac{1}{2} \sum_{j \beta} u_{\lambda i}^{\alpha*}(t) D_{ij}^{\alpha\beta} u_{\lambda j}^\alpha(t) \right] \\ &= \sum_{\lambda i \alpha} \left[\frac{1}{2} \pi_{\lambda i}^{\alpha*} \pi_{\lambda i}^\alpha + \frac{1}{2} \omega_\lambda^2 u_{\lambda i}^{\alpha*} u_{\lambda i}^\alpha \right], \end{aligned} \quad \text{Eq. S43}$$

where $\Pi_{\lambda i}^\alpha(t)$ and $\pi_{\lambda i}^\alpha$ are the momentum and mass-weighted momentum, respectively. The first term is the kinetic energy, and the second term is the potential energy V , which can also be described by $V = \sum_\lambda \frac{1}{2} \mathbf{u}_\lambda^\dagger \mathbf{D} \mathbf{u}_\lambda$.

When computing the phonon frequencies, it is important to impose the acoustic sum rule such that rigid-body motion corresponds to zero frequency. According to the acoustic sum rule, the on-site Hessian is given by, $H_{ii}^{\alpha\beta} = - \sum_{j \neq i} H_{ij}^{\alpha\beta}$. The force constants involving two distinct atoms $H_{ij}^{\alpha\beta}$ ($i \neq j$) can be categorized into two types. If atom i and atom j belong to the same molecule, we call it the intramolecular force constant $\Phi_{ij}^{\alpha\beta}$. Conversely, when atom i and atom j are from different molecules, we call it the intermolecular force constant $\Psi_{ij}^{\alpha\beta}$. Subsequently, we apply the acoustic sum rule to compute the on-site force constants, such that $\Phi_{ii}^{\alpha\beta} = - \sum_{j \neq i} \Phi_{ij}^{\alpha\beta}$ for intramolecular interactions, and $\Psi_{ii}^{\alpha\beta} = - \sum_{j \neq i} \Psi_{ij}^{\alpha\beta}$ for intermolecular interactions. We then have, $\mathbf{H} = \mathbf{\Phi} + \mathbf{\Psi}$, which allows us to define the potential energy due to intramolecular and

intermolecular interactions by $V_{\text{intra}} = \sum_{\lambda} \frac{1}{2} \mathbf{u}_{\lambda}^{\dagger} \mathbf{M} \Phi \mathbf{M} \mathbf{u}_{\lambda}$ and $V_{\text{inter}} = \sum_{\lambda} \frac{1}{2} \mathbf{u}_{\lambda}^{\dagger} \mathbf{M} \Psi \mathbf{M} \mathbf{u}_{\lambda}$. The total potential energy is the sum of these two parts, $V = V_{\text{intra}} + V_{\text{inter}}$. For a specific phonon mode λ , we can define contributions from intramolecular and intermolecular bonds as,

$$\eta_{\lambda, \text{intra}} = \frac{\mathbf{u}_{\lambda}^{\dagger} \mathbf{M} \Phi \mathbf{M} \mathbf{u}_{\lambda}}{\mathbf{u}_{\lambda}^{\dagger} \omega_{\lambda}^2 \mathbf{u}_{\lambda}}, \quad \text{Eq. S44}$$

$$\eta_{\lambda, \text{inter}} = \frac{\mathbf{u}_{\lambda}^{\dagger} \mathbf{M} \Psi \mathbf{M} \mathbf{u}_{\lambda}}{\mathbf{u}_{\lambda}^{\dagger} \omega_{\lambda}^2 \mathbf{u}_{\lambda}}. \quad \text{Eq. S45}$$

It is straightforward to verify that for each phonon mode, $\eta_{\lambda, \text{intra}} + \eta_{\lambda, \text{inter}} = 1$. To illustrate these metrics, we plot $\eta_{\lambda, \text{inter}}$ in Fig. 4.

The thermal average of the normal mode amplitude

The phonon annihilation operator and creation operator are given by⁶²,

$$a_{qv} = \frac{1}{\sqrt{NN_{\text{uc}}}} \sum_{R_{\tau}} \sum_j e^{-i\mathbf{q} \cdot \mathbf{R}_{\tau}} \mathbf{e}_{vj}(\mathbf{q}) \cdot \left[\sqrt{\frac{M_j \omega_v(\mathbf{q})}{2\hbar}} \mathbf{u}_j(\mathbf{R}_{\tau}) + i \sqrt{\frac{1}{2\hbar M_j \omega_v(\mathbf{q})}} \mathbf{p}_j(\mathbf{R}_{\tau}) \right], \quad \text{Eq. S46}$$

$$a_{qv}^{\dagger} = \frac{1}{\sqrt{NN_{\text{uc}}}} \sum_{R_{\tau}} \sum_j e^{i\mathbf{q} \cdot \mathbf{R}_{\tau}} \mathbf{e}_{vj}^*(\mathbf{q}) \cdot \left[\sqrt{\frac{M_j \omega_v(\mathbf{q})}{2\hbar}} \mathbf{u}_j(\mathbf{R}_{\tau}) - i \sqrt{\frac{1}{2\hbar M_j \omega_v(\mathbf{q})}} \mathbf{p}_j(\mathbf{R}_{\tau}) \right], \quad \text{Eq. S47}$$

where N is number of atoms in a unit cell, N_{uc} is the number of unit cells and \mathbf{R}_{τ} is the Cartesian coordinates of the τ th unit cell. Phonons are bosons, and the corresponding annihilation and creation operators obey the relations defined in Eqs. S21, S22 and S23.

The displacements and momenta can be expressed in terms of these operators,

$$\mathbf{u}_j(\mathbf{R}_{\tau}) = \frac{1}{\sqrt{NN_{\text{uc}}}} \sum_{qv} \sqrt{\frac{\hbar}{2M_j \omega_v(\mathbf{q})}} (a_{qv} + a_{-qv}^{\dagger}) \mathbf{e}_{vj}(\mathbf{q}) e^{i\mathbf{q} \cdot \mathbf{R}_{\tau}}, \quad \text{Eq. S48}$$

$$\mathbf{p}_j(\mathbf{R}_{\tau}) = \frac{-i}{\sqrt{NN_{\text{uc}}}} \sum_{qv} \sqrt{\frac{\hbar M_j \omega_v(\mathbf{q})}{2}} (a_{qv} - a_{-qv}^{\dagger}) \mathbf{e}_{vj}(\mathbf{q}) e^{i\mathbf{q} \cdot \mathbf{R}_{\tau}}. \quad \text{Eq. S49}$$

Note that the eigenvectors satisfy the orthogonality and completeness relations,

$$\sum_{j=1}^N \mathbf{e}_{vj}^*(\mathbf{q}) \mathbf{e}_{\mu j}(\mathbf{q}) = \delta_{\nu\mu}, \quad \text{Eq. S50}$$

$$\sum_{\nu}^{3N} e_{\nu j \alpha}^*(\mathbf{q}) e_{\nu k \beta}(\mathbf{q}) = \delta_{\alpha \beta} \delta_{jk}. \quad \text{Eq. S51}$$

Correspondingly, the Hamiltonian is given by,

$$H = \sum_{\mathbf{q}\nu} \hbar \omega_{\nu}(\mathbf{q}) \left(a_{\mathbf{q}\nu}^\dagger a_{\mathbf{q}\nu} + \frac{1}{2} \right), \quad \text{Eq. S52}$$

where $a_{\mathbf{q}\nu}^\dagger a_{\mathbf{q}\nu} = n_{\mathbf{q}\nu}$ is the particle number operator.

The thermal average of the squared amplitude of the displacement is,

$$\begin{aligned} \langle |\mathbf{u}_j(\mathbf{R}_{\tau})|^2 \rangle &= \text{tr} \left(|\mathbf{u}_j(\mathbf{R}_{\tau})|^2 \sum_{n_{\mathbf{q}\nu} \mathbf{q}\nu} \frac{e^{-\frac{n_{\mathbf{q}\nu} \hbar \omega_{\nu}(\mathbf{q})}{k_B T}}}{Z} |n_{\mathbf{q}\nu}\rangle \langle n_{\mathbf{q}\nu}| \right) \\ &= \text{tr} \left[\frac{1}{N_{\text{uc}}} \sum_{n_{\mathbf{q}\nu} \mathbf{q}\nu} \frac{e^{-\frac{n_{\mathbf{q}\nu} \hbar \omega_{\nu}(\mathbf{q})}{k_B T}}}{1 - e^{-\frac{\hbar \omega_{\nu}(\mathbf{q})}{k_B T}}} \frac{\hbar}{2M_j \omega_{\nu}(\mathbf{q})} (a_{\mathbf{q}\nu} a_{\mathbf{q}\nu}^\dagger + a_{\mathbf{q}\nu}^\dagger a_{\mathbf{q}\nu}) \mathbf{e}_{\nu j}^*(\mathbf{q}) \cdot \mathbf{e}_{\nu j}(\mathbf{q}) |n_{\mathbf{q}\nu}\rangle \langle n_{\mathbf{q}\nu}| \right] \\ &= \frac{1}{N_{\text{uc}}} \sum_{\mathbf{q}\nu} \langle 2n_{\mathbf{q}\nu} + 1 \rangle \frac{\hbar}{2M_j \omega_{\nu}(\mathbf{q})} |\mathbf{e}_{\nu j}(\mathbf{q})|^2 \quad \text{Eq. S53} \\ &= \frac{1}{N_{\text{uc}}} \sum_{\mathbf{q}\nu} \frac{\hbar [2n_{\text{BE}}(\omega_{\nu}(\mathbf{q})) + 1]}{2M_j \omega_{\nu}(\mathbf{q})} |\mathbf{e}_{\nu j}(\mathbf{q})|^2 \\ &= \frac{1}{N_{\text{uc}}} \sum_{\mathbf{q}\nu} A_{\mathbf{q}\nu j}^2 |\mathbf{e}_{\nu j}(\mathbf{q})|^2, \end{aligned}$$

where Z is the Canonical partition function and n_{BE} is the Bose-Einstein distribution function. We identify the thermal average of the normal mode's amplitude for j th atom in the unit cell as:

$$A_{\mathbf{q}\nu j} = \sqrt{\frac{\hbar [2n_{\text{BE}}(\omega_{\nu}(\mathbf{q})) + 1]}{2M_j \omega_{\nu}(\mathbf{q})}}. \quad \text{Eq. S54}$$

In the classical limit where $\hbar \omega_{\nu}(\mathbf{q}) \ll k_B T$, we have^{63,64},

$$A_{\mathbf{q}\nu j} \approx \frac{1}{\omega_{\nu}(\mathbf{q})} \sqrt{\frac{k_B T}{M_j}}. \quad \text{Eq. S55}$$

We use Eq. S55 to compute the atomic displacement depicted in Fig. S29.

Intramolecular and intermolecular vibrational modes

For intramolecular vibrational modes, we define three types of motion: rotation, bond length distortion, and angle distortion. For rotation, we compute the angle between the Fe-N bond at equilibrium (ideal structure) and the Fe-N bond when atoms are displaced according to a phonon eigenmode. Given the six Fe-N bonds, we use the largest rotation angle among these bonds as the rotation metric, $R = \max[\arccos(\overrightarrow{\text{Fe-N}}_{\text{eq}} \cdot \overrightarrow{\text{Fe-N}}_{\text{disp.}})]$. For bond length distortion, we use the standard deviation of the Fe-N bonds divided by their mean as the metric $L = \text{std}(|\overrightarrow{\text{Fe-N}}_{\text{disp.}}|)/\text{mean}(|\overrightarrow{\text{Fe-N}}_{\text{disp.}}|)$, which is a dimensionless quantity. For angle distortion, we consider the N-Fe-N angle, where the two N atoms are adjacent and both bonding to the same Fe atom. There are 12 N-Fe-N angles in total. For an ideal octahedron, the N-Fe-N angle is 90° . For the $\text{Fe}[\text{HB}(\text{tz})_3]_2$ molecule at its equilibrium position, the N-Fe-N angles slightly deviate from 90° . They range from 88° to 92° in the LS phase and from 84° to 92° in the HS phase. When a phonon mode is excited, the N-Fe-N angle can further deviate from 90° . Here, we use the standard deviation of all 12 N-Fe-N angles, denoted as $A = \text{std}(\angle \text{N-Fe-N})$, to represent the degree of angle distortion.

For intermolecular vibrational modes, we focus on the N--B hydrogen bond. Upon the excitation of a phonon mode, the N-H hydrogen bond deviates from its equilibrium position. We use the mean of the angle between the N--H bond with and without the phonon excitation as the metric of angle distortion, given by $R = \text{mean}[\arccos(\overrightarrow{\text{N--H}}_{\text{eq}} \cdot \overrightarrow{\text{N--H}}_{\text{disp.}})]$. The lengths of N--H bonds also change. Therefore, we use the average length of all N--H bonds $L = \text{mean}(|\overrightarrow{\text{N--H}}_{\text{disp.}}|)$ as an indicator. Since the N--H bond length varies depending on its local atomic environments, we use the standard deviation of all N--H bond lengths $S = \text{std}(|\overrightarrow{\text{N--H}}_{\text{disp.}}|)$ as the metric to evaluate the length variation among hydrogen bonds.

In Fig. S29a, we observe that rotation of the Fe-N bonds is involved in most phonon modes. The rotation angle increases with decreasing phonon frequency. The lengths of Fe-N bonds exhibit greater variability when phonons are excited. In particular, low-energy phonons tend to cause a more pronounced and nonuniform stretching of the Fe-N bonds compared to high-energy phonons. Additionally, there is a greater degree of length distortion in Fe-N bonds of the HS structure compared to the LS. Interestingly, the N-Fe-N angles remain largely unchanged from the equilibrium structure, suggesting that bending of a Fe-N polygon is a more energetically costly process than stretching or rotating. Fig. S29b indicates that hydrogen bonds undergo greater rotation under the influence of lower-energy phonons. The average length of hydrogen bonds is almost the same as the equilibrium limit for both LS and HS phases. However, the length of each individual hydrogen bond changes differently, leading to a large standard deviation of the hydrogen bond length. This standard deviation of hydrogen bonds becomes more elevated as the phonon energy decreases. Although at equilibrium the standard deviation of hydrogen bond lengths is slightly smaller in the HS phase than that in the LS phase, certain low-energy phonons can induce an even larger variance in the HS phase.

Specifically, to quantify the libration dynamics of N--H hydrogen bonds, we evaluate the mean of the squared angular displacements $\langle \theta^2 \rangle$. The libration potential energy can be described by a harmonic form, $V(\theta) = \frac{1}{2}k\theta^2$, where k is the torsional force constant. Since the harmonic force constants between the LS and HS phases vary only slightly (Fig. 4), we use the normalized

difference $\frac{\langle \theta_{\text{HS}}^2 - \theta_{\text{LS}}^2 \rangle}{\langle \theta_{\text{LS}}^2 \rangle}$ to characterize the enhancement of librations in the HS phase. As shown in Fig. S29c, the hydrogen bonds for most optical phonon modes below 12 THz exhibit more librational character (hence less bond-stretching vibrational character), with an average increase in $\langle \theta^2 \rangle$ of up to 85%.

To summarize, the atomic displacements due to different phonon modes involve more rotation and length distortion of Fe–N bonds rather than any bending within the Fe–N polygon. Additionally, they involve rotation and length distortion of N---H hydrogen bonds. The rotation of Fe–N bonds is similar for the LS and HS phases, whereas the length distortion of Fe— bonds is much higher in the HS phase compared to the LS phase. This is expected as the most significant change in the bond strength during the SCO transition occurs in the metal-ligand bonds (Fig. 4). The N---H bonds involve considerably more libration motions in the HS phase than in the LS phase.

The molecular orbitals from DFT

All molecular orbital calculations were performed by DFT⁶⁵ as implemented in the Jaguar 9.1 suite⁶⁶ of ab initio quantum chemistry programs. In the calculation, the molecular structure of Fe[HB(tz)₃]₂ obtained from the single-crystal structure of Fe[HB(tz)₃]₂ at 320 K was used as an initial structure. Geometry optimizations to the stationary points were performed with the B3LYP^{67–70} hybrid exchange and correlation functional including Grimme's D3 dispersion correction⁷¹. The 6-31G** basis set⁷² was used for all atoms except for Fe, which was represented by the Los Alamos LACVP** basis set^{73–75}, including effective core potentials. The HOMO and LUMO energies of the optimized structures were reevaluated by single-point calculations on each optimized geometry using Dunning's correlation consistent triple-z basis set cc-pVTZ(-f)⁷⁶ that includes a double set of polarization functions. The Fe atom was represented by using a triple-z version of LACVP**, where the exponent of the basis functions was decontracted to mimic the flexibility of the triple-z basis. We employed the standard set of optimized radii in Jaguar for H (1.150 Å), B (2.042 Å), C (1.900 Å), N (1.600 Å), and Fe (1.456 Å)⁷⁷.

Raman scattering

We used L-cysteine to benchmark our Raman scattering measurements (using a Horiba LabRam Evolution Raman spectrometer with an excitation wavelength of 633 nm) with an ultra-low frequency filter. The differential cross sections of Stokes and anti-Stokes Raman scattering in the same material are given by, $I_{\text{Stokes}} \propto \frac{n+1}{\omega_v} \text{DOS}(\omega)$ and $I_{\text{anti-Stokes}} \propto \frac{n}{\omega_v} \text{DOS}(\omega)$, respectively, where n is the Bose-Einstein distribution function, ω_v is the phonon frequency and v is the phonon branch index. In Fig. S32a, we show the Stokes and anti-Stokes Raman scattering intensity without baseline subtraction, and we find that the intensity of the Stokes Raman scattering is slightly larger than the anti-Stoke scattering. The ratio of the Stokes and anti-Stokes Raman scattering intensities roughly follows the curve given by $\frac{n+1}{n}$ except the peak around 7 cm⁻¹. We believe this peak is not intrinsic to the material but due to imperfect filtering or a slight line shift in the laser source. The other two peaks around 10 cm⁻¹ and 15 cm⁻¹ align well with reported values, providing confidence in the accuracy of the Raman scattering measurement. In the data analysis for our sample, we only consider data with a Raman shift larger than 10 cm⁻¹ to exclude the false peak around 7 cm⁻¹. In addition, since the baselines are similar for both Stokes and anti-Stokes Raman scattering, we use the Stokes Raman scattering intensity to study the vibrational properties of Fe[HB(tz)₃]₂ because of the slightly higher signal-to-noise ratio.

Modeling the spin-crossover transition including effect of lattice vibrations

We mainly follow the phenomenological model proposed by Zimmerman and König⁷⁸ to describe the fraction of HS Fe centers versus temperature and the details of the our modeling are provided in the following. We start with the canonical partition function in the HS phase given by,

$$Z = \sum_i e^{-\beta E_i}, \quad \text{Eq. S56}$$

where $\beta = 1/k_B T$ and E_i is the electronic energy level. The Gibbs free energy per metal center is given by,

$$G = (\Delta E - k_B T \ln Z)n_{\text{HS}} - Jn_{\text{HS}}^2 + k_B T[n_{\text{HS}} \ln n_{\text{HS}} + (1 - n_{\text{HS}}) \ln(1 - n_{\text{HS}})], \quad \text{Eq. S57}$$

where ΔE is the energy difference between the LS and HS states, n_{HS} is the fraction of HS Fe centers and J is the interaction constant for the HS Fe center, which is larger as the interaction between the LS Fe centers and HS Fe centers is stronger. Accordingly, J also serves as a measure for cooperativity⁷⁹. The last term in Eq. S57 arises from the configurational entropy. The key assumption made by Zimmerman and König is that Z is a temperature-independent constant. This is a reasonable assumption when other terms in the Gibbs free energy play a more important role in changing n_{HS} .

At thermal equilibrium, the condition $\frac{\partial G}{\partial n_{\text{HS}}} = 0$ leads to the following implicit equation,

$$n_{\text{HS}} = \frac{Z}{Z + e^{\beta(\Delta E - 2Jn_{\text{HS}})}}. \quad \text{Eq. S58}$$

We can numerically solve this equation to obtain n_{HS} at a given temperature T . Specifically, at the critical temperature T_c , we have $n_{\text{HS}}(T_c) = 1/2$, which means $Z = e^{(\Delta E - J)/k_B T_c}$.

We now proceed to include the contribution of the phonon entropy to the Gibbs free energy. The Gibbs free energy is expressed as,

$$G = (\Delta E - k_B T \ln Z)n_{\text{HS}} - Jn_{\text{HS}}^2 + k_B T[n_{\text{HS}} \ln n_{\text{HS}} + (1 - n_{\text{HS}}) \ln(1 - n_{\text{HS}})] - TS_{\text{ph}}, \quad \text{Eq. S59}$$

where S_{ph} is the phonon entropy. Zimmerman and König used a sophisticated approach to include effect of the lattice vibrations using Debye model⁷⁸. However, as shown in Fig. S23, we find that the phonon entropy can be well approximated by $S_{\text{ph}} \approx A + BT + Cn_{\text{HS}} + DTn_{\text{HS}}$. When further taking the derivative of the Gibbs free energy in Eq. S59, the first two terms disappear. The third term can be lumped into Z , and we only need to consider the fourth term. In other words, we only introduce a third parameter to the original model, which is more tractable than Zimmerman and König's method. The implicit equation that governs n_{HS} becomes,

$$n_{\text{HS}} = \frac{Ze^{DT/k_B}}{Ze^{DT/k_B} + e^{\beta(\Delta E - 2Jn_{\text{HS}})}}. \quad \text{Eq. S60}$$

At the critical temperature, we obtain the modified condition, $Z = e^{\frac{(\Delta E - J)}{k_B T_c} - \frac{DT_c}{k_B}}$.

Next, we extract the parameters in the model by fitting them to the experimental data from SQUID. We notice that the fitting of J is not sensitive to the choice of ΔE . Therefore, we set $\Delta E = 0.1$ eV as a constant and choose J and D as fitting parameters. As shown in Fig. S33, our model can well capture the essential features of SCO transition. In $\text{Fe}[\text{HB}(\text{tz})_3]_2$, we find $J = 56.1$ meV, $D/k_B = 0.051$ K $^{-1}$ for the heating process and $J = 54.4$ meV, $D/k_B = 0.045$ K $^{-1}$ for the cooling process. It is worth noting that the order of magnitude of J matches the thermal energy $k_B T_c = 28.6$ meV, which implies an underlying relationship between cooperativity and phase transition temperature.

Single crystal X-ray diffraction

Variable-temperature unit cell parameters and single crystal structures were determined using a single crystal mounted in silicone grease with a MiTeGen MicroMounts™. All experiments were performed using a Bruker D8 VENTURE single-crystal diffractometer with Mo/Cu I μ S microfocus X-ray sources, PHOTON III-C14 detector, and an Oxford Cryosystems Cryostream cryostat at Harvard University. Data were integrated and absorption corrections were applied using Bruker APEX5 software¹. The space groups of each compound were determined by examination of systematic absences, E-statistics, and successive refinement of the structure. Using the OLEX2 interface⁸⁰, the structures were solved with intrinsic phasing (SHELXT)⁸¹ methods and further refined using least squares minimization with SHELXL⁸². Thermal parameters for all non-hydrogen atoms were refined anisotropically. All hydrogen atoms were fixed at ideal positions, refined using a riding model for all structures, and refined using isotropic displacement parameters derived from their parent atoms. The unit cell parameters presented in Fig. S34 were determined using data where $I/\sigma \geq 3$ in Bruker APEX5 software. The unit cell volume data were subsequently used to calculate the volumetric heat capacity shown in Fig. S36.

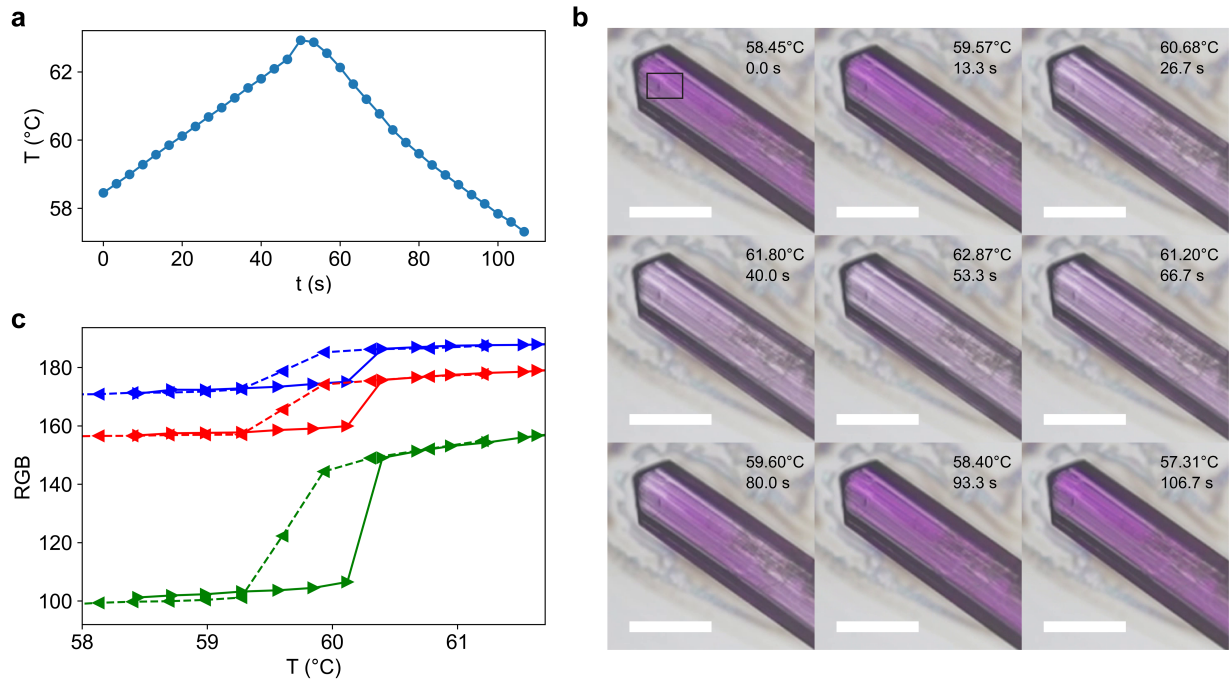


Fig. S1 | Fe[HB(tz)₃]₂ single crystal for FDTR measurements. **a**, The time trajectory of the temperature of the INSTECH hot and cold stage during heating and cooling under vacuum. **b**, Optical microscope images at various temperatures of an Fe[HB(tz)₃]₂ deposited on a Si wafer show a color change from purple to pearl pink as the temperature passes the SCO transition temperature, which agrees with prior reports²⁶. Scale bars, 200 μm . **c**, The average RGB values of the selected area on the sample surface (marked by the black box in **b**) exhibit abrupt changes near the phase transition temperature. The solid and dashed lines correspond to the heating and cooling process. Note that the temperature reading from the sample stage is likely higher than the actual sample temperature due to the combined thermal resistance of the Si substrate and the carbon tape, as well as radiation heat loss to surroundings. For FDTR measurements, silver paste was used instead of carbon tape to minimize this thermal resistance.

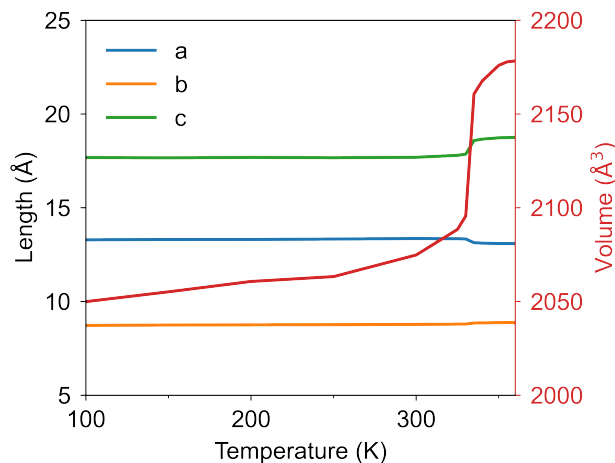


Fig. S2 | Variable temperature unit cell dimensions. The lattice constants of $\text{Fe}[\text{HB}(\text{tz})_3]_2$ are plotted as a function of temperature. The relative volume change from low spin (LS) to high spin (HS) near the transition temperature is about 3%, and the largest change in dimensions is along the crystallographic *c* axis, which corresponds to the *z*-direction (perpendicular to the Si substrate) for all FDTR measurements. The unit cell data are from single-crystal X-ray diffraction (XRD) results previously reported in Ref.⁴¹.

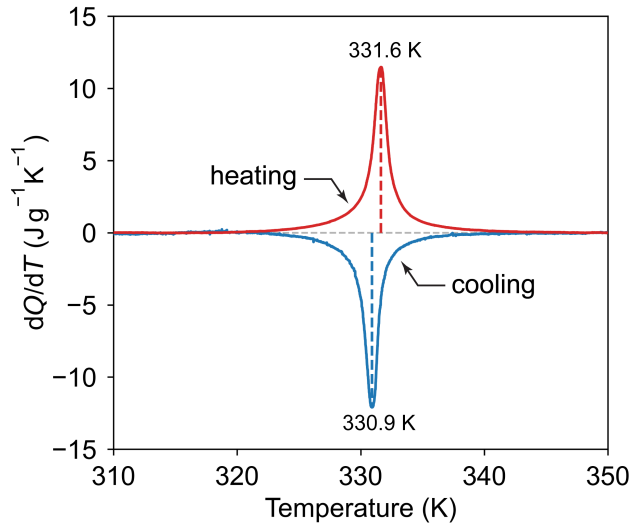


Fig. S3 | Differential scanning calorimetry. The heating and cooling rates are set at 1 K min^{-1} . Heating (red) and cooling (blue) DSC traces were obtained by subtracting the measured data with cubic spline baselines. The phase transition temperatures, determined by the peak positions on the dQ/dT curve (dashed lines), are $T_{\text{tr}} = 331.6 \text{ K}$ for heating and $T_{\text{tr}} = 330.9 \text{ K}$ for cooling, differing by only 0.7 K. The low hysteresis observed is intrinsic to the SCO transition. The enthalpy change $\Delta H(T)$ associated with the SCO transition was obtained from the cumulative integration of dQ/dT . The entropy change during the heating-induced SCO transition, presented in Fig. 1e, was obtained by $\Delta S(T) = \Delta H(T)/T_{\text{tr}}$.

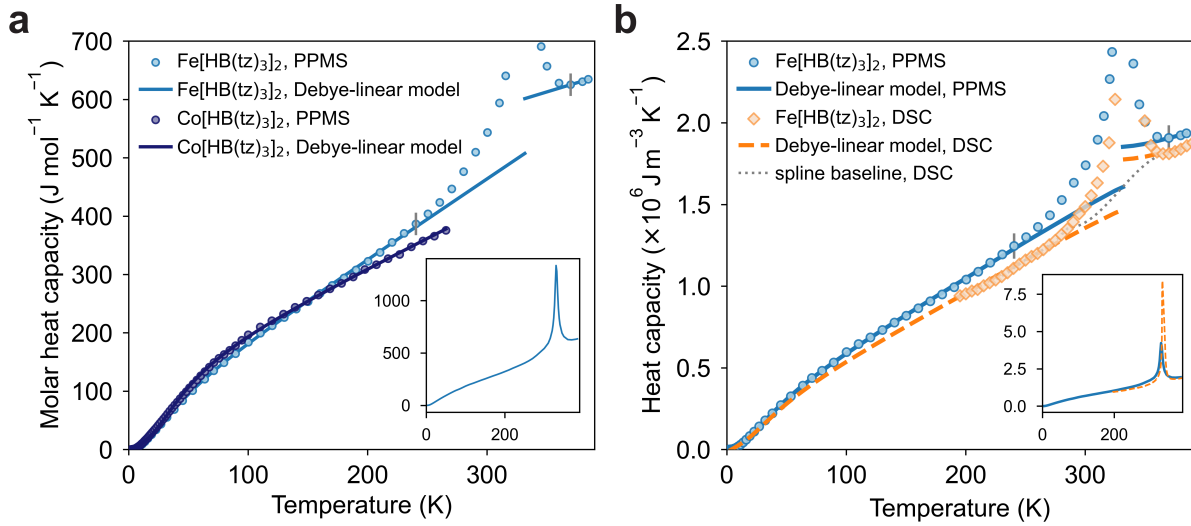


Fig. S4 | Heat capacity. **a**, The experimentally measured heat capacity of $\text{Fe}[\text{HB}(\text{tz})_3]_2$ and $\text{Co}[\text{HB}(\text{tz})_3]_2$ using a PPMS (blue circles) and lattice heat capacity (blue line) using a model that combines a Debye model with a linear-in- T term. As pointed out by Rafizadeh and Yip⁸³, the Debye model can only describe the lattice composed of rigid molecules, and a linear term is necessary to account for internal mode contributions. The chosen functional form of the model accurately describes the temperature dependence of the heat capacity in both complexes. Inset: full PPMS data. **b**, The volumetric heat capacity of $\text{Fe}[\text{HB}(\text{tz})_3]_2$, calculated from the molar heat capacity divided by the molar volume. The heat capacity from DSC is fit by the same model (dashed line) that was used for the PPMS data multiplied by a different scaling factor for the LS and HS phases. The heat capacity baseline using a cubic spline is represented as a grey dotted line. Though there is a small difference in the measured heat capacity of the HS phase between the PPMS and DSC data, these differences do not lead to any significant changes in the thermal conductivity that is determined by fitting FDTR data (see Fig. S5). Inset: full DSC and PPMS data.

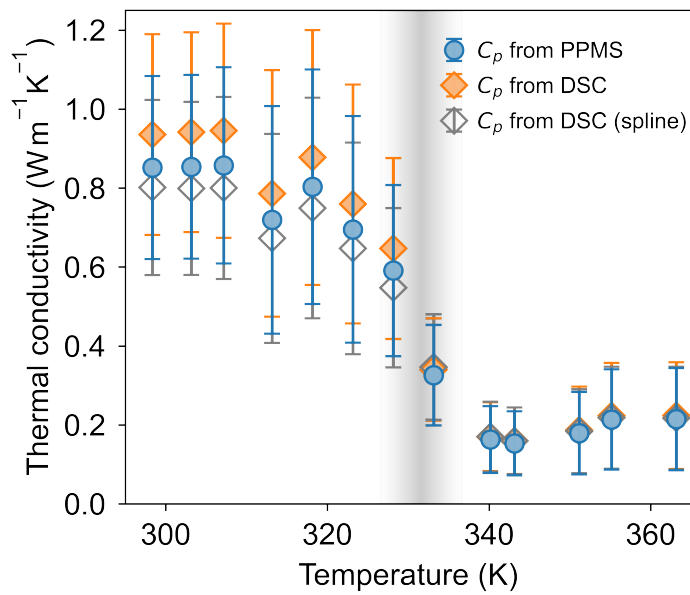


Fig. S5 | Effect of heat capacity on thermal conductivity fits. The blue circles, orange diamonds and gray diamonds represent the best fits to FDTR data using heat capacity data determined by the Debye-linear model from PPMS data, the Debye-linear model from DSC data, and the cubic spline from DSC data, respectively, which are in good agreement.

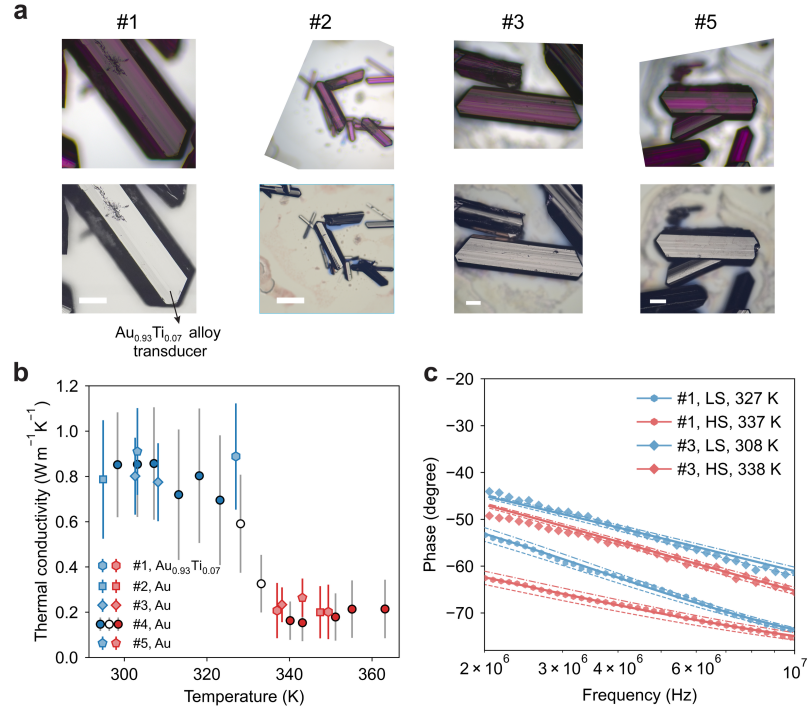


Fig. S6 | Reproducibility of thermal conductivity changes in $\text{Fe}[\text{HB}(\text{tz})_3]_2$. **a**, Brightfield microscopy images of measured samples (see Fig. 2 for sample #4). The top and bottom rows show the samples before and after metal transducer deposition, respectively. All scale bars represent 100 μm . **b**, Thermal conductivity results for a single crystal of $\text{Fe}[\text{HB}(\text{tz})_3]_2$ coated with a $\text{Au}_{0.93}\text{Ti}_{0.07}$ alloy transducer layer (sample #1) and for 4 independent single crystals of $\text{Fe}[\text{HB}(\text{tz})_3]_2$ coated with an Au transducer layer (samples #2, #3, #4 and #5). Note that the data for sample #4 is shown in Fig. 1, and sample #5 is used for the cycling test illustrated in Fig. 2. **c**, The phase lag data (circles) for the LS and HS phases of sample #1 and #3. Solid lines indicate the best fits, while dashed and dash-dotted lines correspond to -20% and $+20\%$ variations of the thermal conductivity, respectively. The lower thermal conductivity of the alloy transducer compared to the Au transducer enhances the sensitivity of the FDTR measurement to the thermal conductivity differences between LS and HS phases.

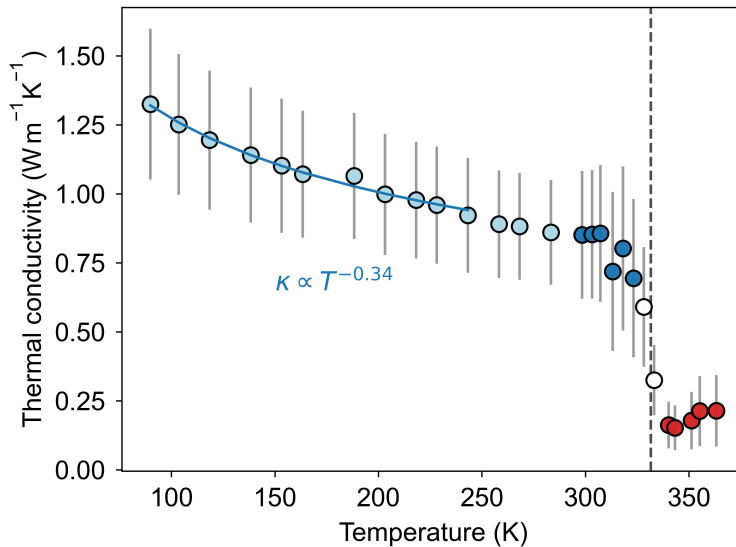


Fig. S7 | Low-temperature thermal conductivity data. The thermal conductivity of Fe[HB(tz)₃]₂ determined from FDTR experiments over a wide temperature range. Note that the light blue circles correspond to a single crystal sample with a gold transducer layer that was deposited by sputtering, while the remaining circles correspond to a single crystal sample with a gold transducer layer that was deposited by e-beam evaporation. The dashed vertical line corresponds to the SCO transition temperature ($T_{\text{tr}} = 331.6$ K). At sub-ambient temperatures—where the Debye + linear-in- T model does not deviate from the experimental heat capacity ($T < 250$ K, as indicated in Fig. 1d)—the thermal conductivity decays as $T^{-0.34}$, which implies that the phonon gas model ($\kappa \propto T^{-1}$) alone is insufficient to describe the observed temperature dependence. This suggests that phonon tunneling is contributing as a weakly temperature-dependent component of the total thermal conductivity.

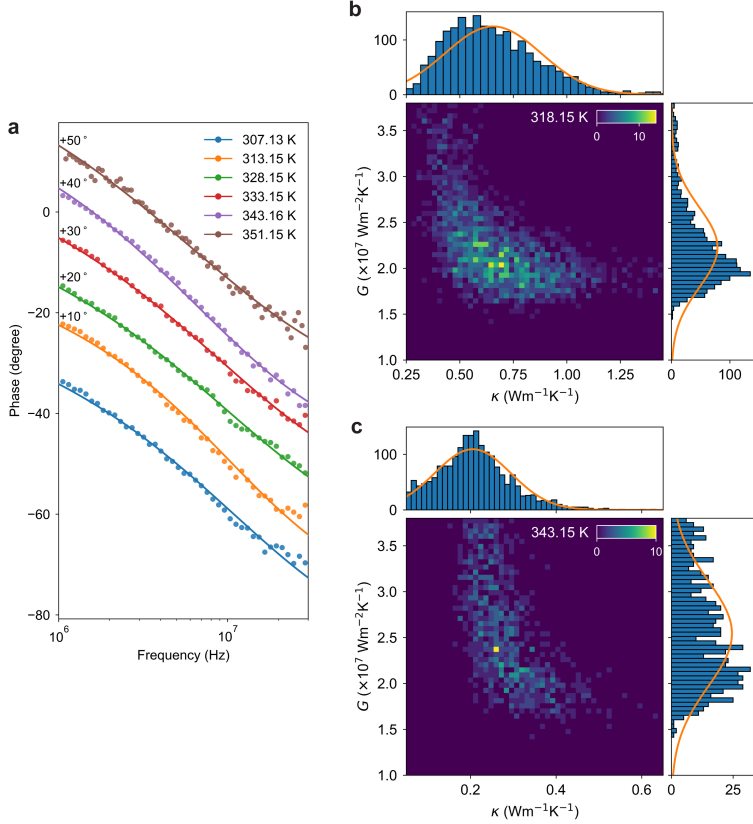


Fig. S8 | FDTR error analysis. **a**, Phase lags for the single crystal of $\text{Fe}[\text{HB}(\text{tz})_3]_2$ that was used to collect the data displayed in Fig. 1 of the manuscript. The plot shows the FDTR experimental data (dots) and best fits (solid lines) at different temperatures. Note that the phase lags are offset vertically by the amounts indicated above each curve to improve clarity. **b,c**, Histograms of the best fits of thermal conductivity, κ , and thermal boundary conductance, G , from repeated random sampling for the LS phase at 318.15 K (**b**) and the HS phase at 343.15 K (**c**). A total of 2,000 samples were used for the simulation at each temperature, with the color indicating the frequency of a certain combination of κ and G . In each sample, we randomly vary all parameters—including the thermal conductivity of the gold transducer layer, the thickness of the gold transducer layer, the heat capacity of the sample, and the effective beam radius—according to a normal distribution with a 5% uncertainty, except the fitting variables (in this case, κ and G). When projecting all data points onto one axis, we can obtain the distribution of the fitting variable along that axis (blue histogram bars). We can represent the projected histograms with normal distributions (orange curves), each having the same mean and standard deviation as the respective set of projected data. The mean and standard deviation at each temperature point are plotted in Fig. 1. It is worth noting that the distributions of G at both temperatures appear slightly skewed, deviating from a symmetric normal distribution. This is a consequence of the low sensitivity to G and the correlation between κ and G that is intrinsic to this multivariate fitting problem. Nonetheless, the mean and standard deviation are still well-defined quantities that inform us of the statistical behavior of the measured transport properties.

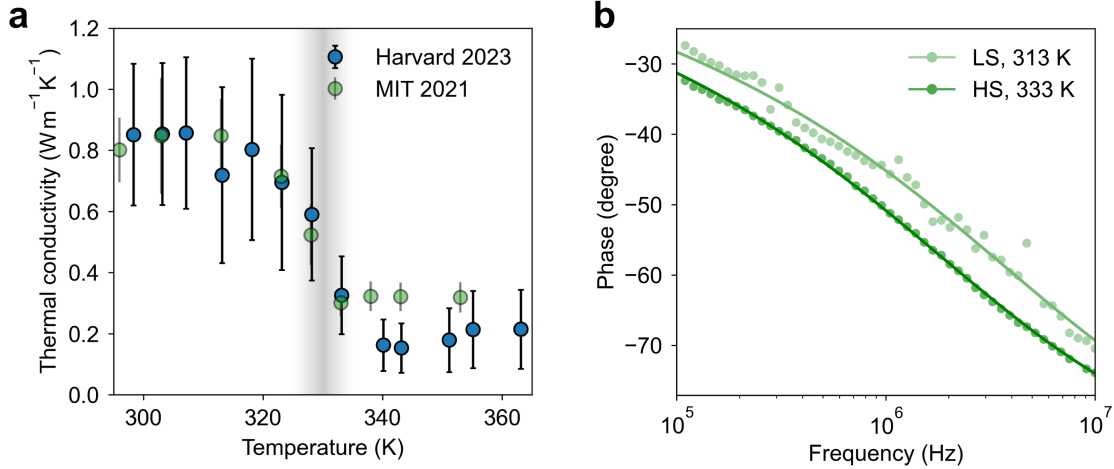


Fig. S9 | Comparison of thermal conductivity data for $\text{Fe}[\text{HB}(\text{tz})_3]_2$ measured on two FDTR instruments. **a**, Thermal conductivity data for two independently synthesized $\text{Fe}[\text{HB}(\text{tz})_3]_2$ samples. The MIT samples were from a 2021 batch, while the Harvard samples were from a batch synthesized in 2023. The FDTR setup at MIT is custom built and uses a 405-nm pump laser. The effective beam radius is approximately 6 μm . The cryostat used at MIT was a MicrostatHe model from Oxford Instruments, operating under atmospheric pressure. For the data from MIT, thermal conductivity and beam radius were fit using both amplitude and phase of the thermoreflectance. We believe these experimental and fitting differences contribute to the differences between the two measurements. **b**, Representative FDTR phase data with corresponding best-fit curves. The noisier data in the LS phase likely results from large temperature-induced thermal expansion when a low modulation frequency is applied.

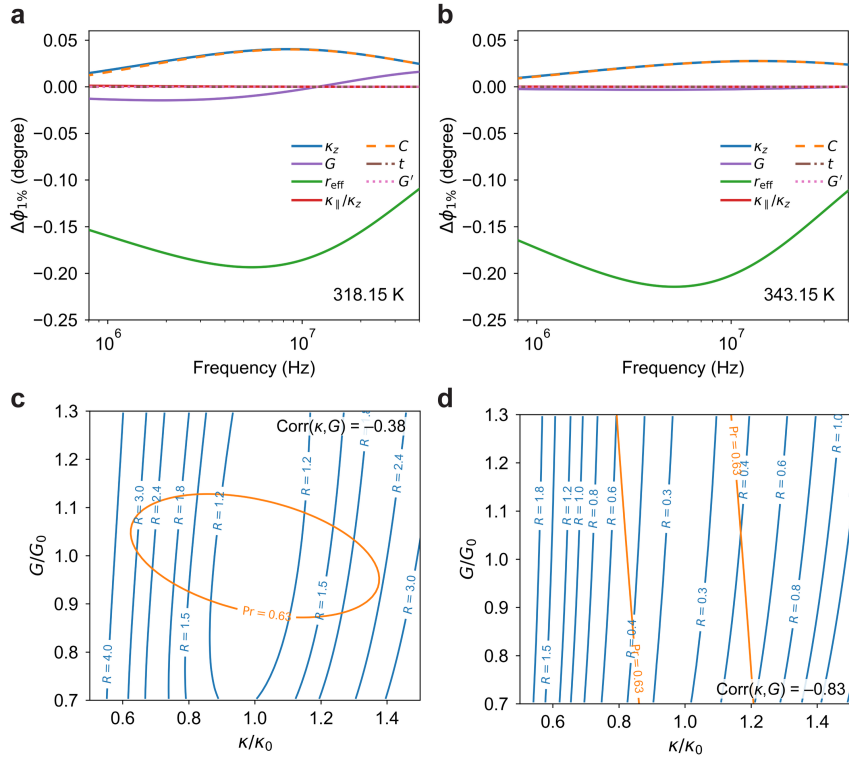


Fig. S10 | Sensitivity and uncertainty analysis for FDTR fitting of Fe[HB(tz)₃]. **a,b**, The sensitivity vector for the thermal boundary conductance between the gold transducer layer and sample, G , the cross-plane thermal conductivity in sample, κ_z , the ratio $\kappa_{\parallel}/\kappa_z$, the thickness of sample, t , the thermal boundary conductance between the sample and the silicon substrate, G' , and the effective beam radius, r_{eff} for the LS (**a**) and HS (**b**) phases. We observe very low sensitivity to fitting in-plane thermal conductivity κ_{\parallel} and negligible sensitivity to the sample thickness t and the interfacial thermal conductance G' , both in the LS and HS phases. Note that the plot shows $\Delta\phi_{1\%} = \frac{\partial\phi}{\partial x_i} \times (0.01x_{0,i})$, which is the finite difference in the phase lag when changing the variable x_i from its best fit $x_{0,i}$ relatively by 1% (which is proportional to the sensitivity vector $\frac{\partial\phi}{\partial x_i}$). The sensitivity to thermal conductivity and heat capacity are almost the same, suggesting that the measurement is actually sensitive to the effusivity $\sqrt{\kappa_z C}$ rather than κ_z or C individually⁵⁸. **c,d**, The confidence interval of $\alpha = 0.63$ (within the orange ellipsoid) overlaid on the sum of squared residuals $R(\kappa, G)$ (blue contour lines) for the LS (**c**) and HS (**d**) phases. From the local curvature of $R(\kappa, G)$ near (κ_0, G_0) , we see that the sensitivity to the cross-plane thermal conductivity κ is much higher than the thermal boundary conductance G . From the confidence interval, we identify a certain degree of correlation between κ and G , as the principal axes are not exactly along the x- and y- axes. In the LS phase, they are slightly anti-correlated, and in the HS phase they are anti-correlated. The correlations, given by $\text{Corr}(\kappa, G) = \frac{\Sigma(\kappa, G)}{\sqrt{\Sigma(\kappa, \kappa) \cdot \Sigma(G, G)}}$ (Σ is the variance-covariance matrix), are -0.38 and -0.83 in the LS and HS phases, respectively. Note that we have divided the sum of squared residuals by the number of frequency points N_{ω} in **c** and **d**.

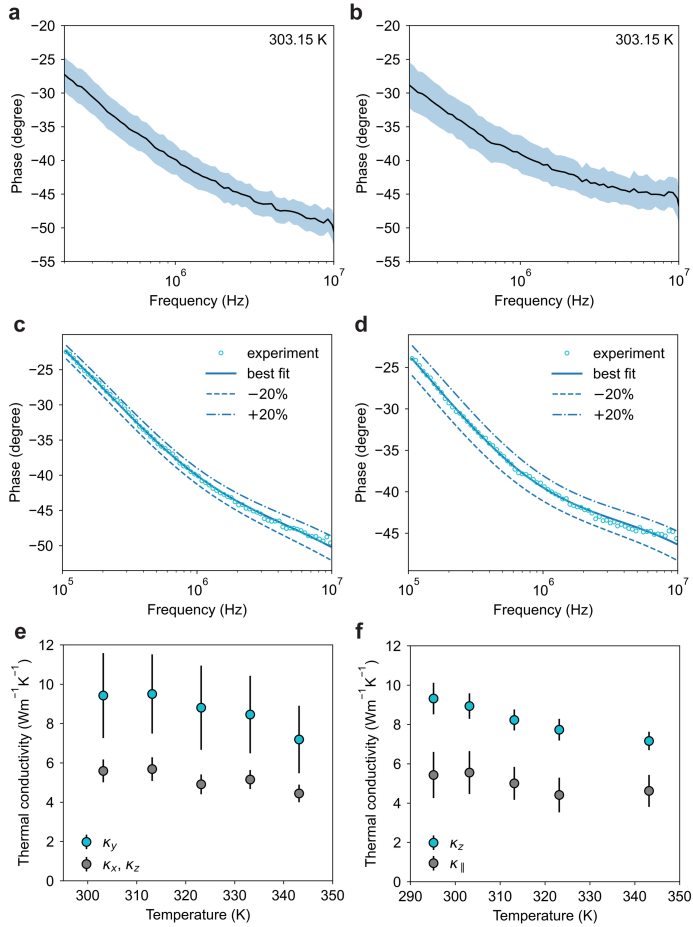


Fig. S11 | Characterization of anisotropic thermal transport in X-cut and Z-cut quartz using a 73-nm Au_{0.93}Ti_{0.07} alloy transducer. **a,b**, The averaged phase lags from 30 consecutive frequency sweeps at 303 K in X-cut (**a**) and Z-cut (**b**) quartz, where the shaded area represents the standard deviation. The variations among different measurements are due to the coefficient of thermoreflectance of Au_{0.93}Ti_{0.07} alloy being one order of magnitude lower than that of Au. The pump and probe power is 4.4 mW and 3 mW, respectively. **c,d**, The experimental data and best fits at 303 K for X-cut (**c**) and Z-cut (**d**) quartz. The dashed and dash-dotted lines correspond to varying κ_z by -20% and +20%. Note that in X-cut quartz, the thermal conductivity is isotropic in the x-z plane, and in Z-cut quartz, it is isotropic in the x-y plane. As a consequence, there are only two independent thermal conductivity components in both cases. In addition to these two thermal conductivity components, we also fit the interfacial thermal conductance between the alloy transducer layer and quartz. **e,f**, The anisotropic thermal conductivity at various temperatures in X-cut (**e**) and Z-cut (**f**) quartz. Our measurements match prior studies⁵³, which found the thermal conductivity in quartz at room temperature is 10.7 W m⁻¹ K⁻¹ parallel to the z-axis and 6.2 W m⁻¹ K⁻¹ perpendicular to the z-axis. The error bars were obtained by running Monte Carlo simulations assuming all parameters except the fitting variables have a 5% uncertainty. The interfacial thermal conductances in both X-cut and Z-cut quartz were found to be 1.7×10^8 W m⁻² K⁻¹ with negligible variations across the temperature range studied in the experiment.

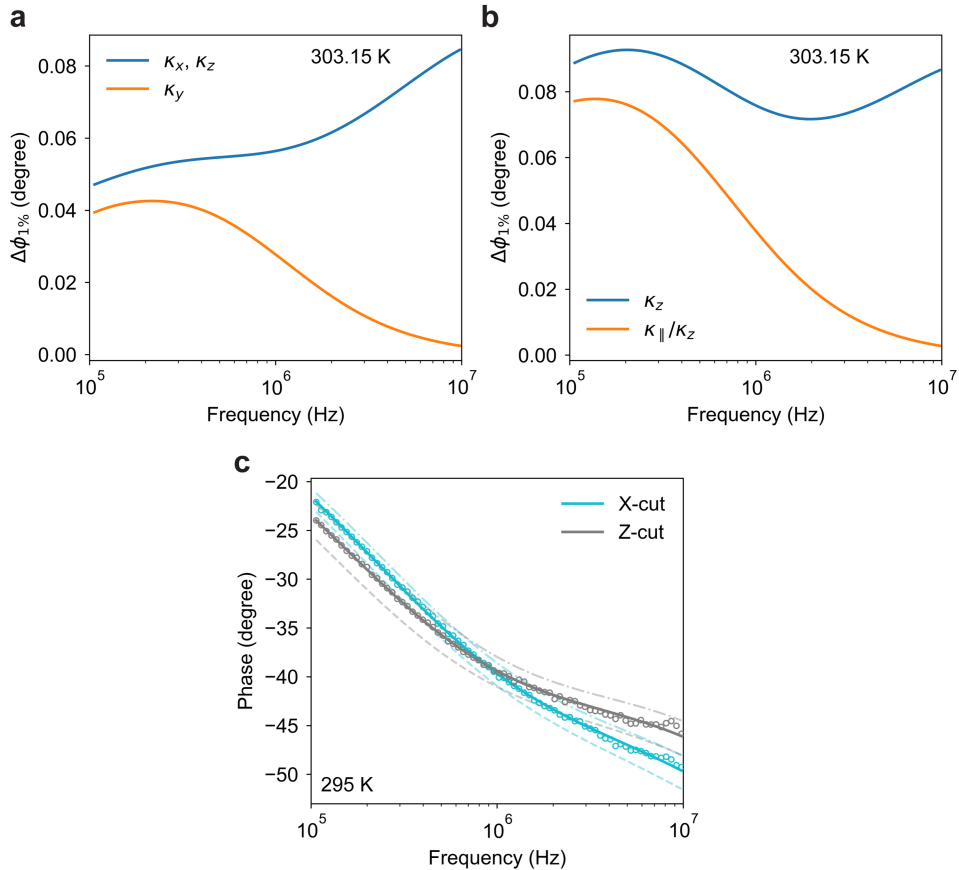


Fig. S12 | The sensitivity to anisotropic thermal conductivity using $\text{Au}_{0.93}\text{Ti}_{0.07}$ alloy transducers. **a,b,** The change in phase lag upon changing the thermal conductivity or the ratio of in-plane and cross-plane thermal conductivity by 1% in X-cut quartz (**a**) and Z-cut quartz (**b**). Note that if using an Au transducer layer, the sensitivity to any in-plane thermal conductivity component is extremely small. In contrast, the alloy transducer improves the sensitivity to in-plane thermal conductivity, making it comparable to that for cross-plane thermal conductivity. **c,** The phase lag in X-cut and Z-cut quartz at 295 K shows a distinctive frequency dependence due to crystal orientation. The dashed and dash-dotted lines correspond to the curves when changing κ_z by -20% and +20%, respectively.

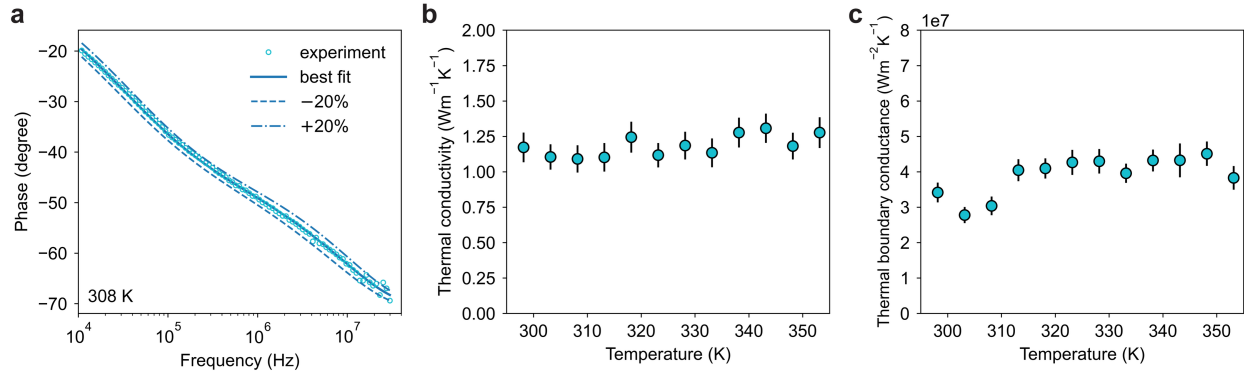


Fig. S13 | Characterization of thermal transport in Corning EAGLE glass. **a**, The best fit from the heat diffusion model and experimental data at 308 K. The dashed and dash-dotted lines correspond to the curves when changing κ_z by -20% and +20%. The pump power was 4.4 mW and the probe power was 3 mW. Notably, the noise level in the phase lag is significantly lower in glass than in quartz. This is due to the lower thermal conductivity of glass, which results in the amplitude of the signal being much larger than the noise. **b**, The thermal conductivity in Corning EAGLE glass at various temperatures. Our measurement agrees relatively well with the value of $\kappa = 1.09 \text{ W m}^{-1} \text{ K}^{-1}$ reported by Corning at 300 K. **c**, The thermal boundary conductance between the alloy transducer and the glass. The error bars were obtained by the Monte Carlo simulations where all parameters except the fitting variables are randomized with a 5% uncertainty.

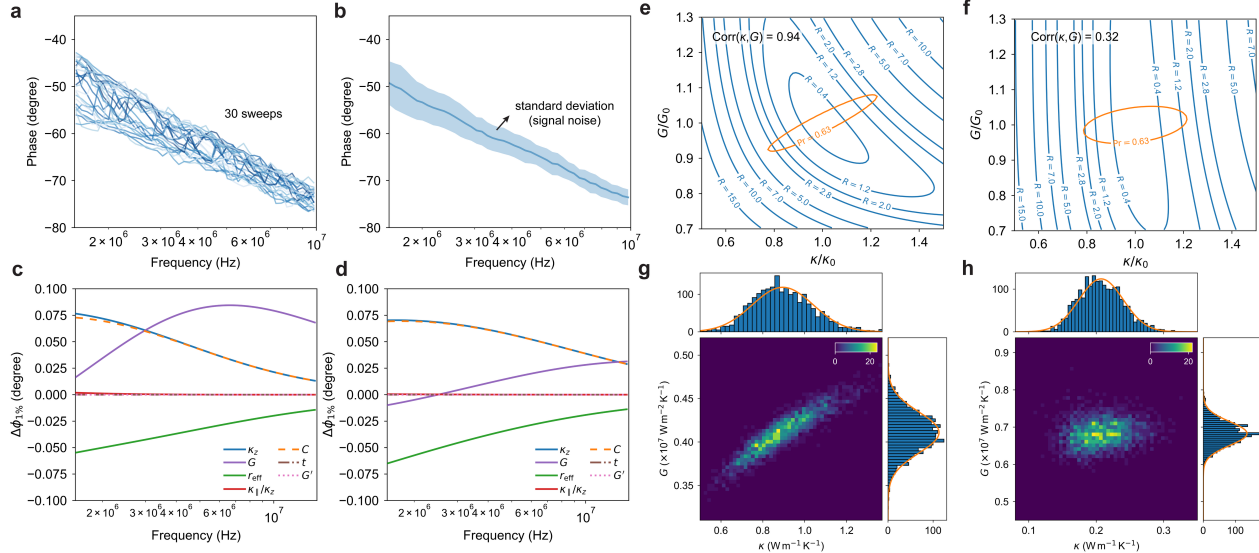


Fig. S14 | Characterization of thermal transport of an $\text{Fe}[\text{HB}(\text{tz})_3]_2$ crystal with a $\text{Au}_{0.93}\text{Ti}_{0.07}$ alloy transducer. **a**, The phase lag data from 30 consecutive frequency sweeps at 327 K. **b**, The averaged phase lag (solid line) and the standard deviation (shaded area), representing the variations due to noise. The noise in the phase lag is greater for the alloy transducer than for the gold transducer because the alloy's thermoreflectance coefficient is an order of magnitude lower than that of gold. To ensure adequate signal, we increased both the pump and probe power to 5 mW. The increased laser heating (including the DC part of the probe laser) can significantly raise the actual temperature of the sample above the nominal temperature set by the temperature stage. As a result, we observed that the SCO transition occurred between nominal temperatures of 273.15 K and 283.15 K, and therefore, we estimate a 53.85 K temperature shift due to laser heating. **c,d**, The sensitivity analysis for the LS phase at 327 K (**c**) and HS phase at 337 K (**d**) using the alloy transducer. The sensitivity to the thermal conductivity using the alloy transducer is overall much higher compared to the gold transducer (Fig. S10). **e,f**, The residual map (blue contours) and confidence interval (orange line) for the LS and HS phases. The correlation between thermal conductivity κ and thermal boundary conductance G are 0.94 and 0.32 for the LS and HS phases, respectively. The confidence interval contour shows a reduced uncertainty in thermal conductivity with the alloy transducer compared to the case of using a gold transducer (Fig. S10). **g,h**, Histograms of the best fits of thermal conductivity κ and thermal boundary conductance G from the Monte Carlo simulations of 2000 samples for the LS (**g**) and HS (**h**) phases.

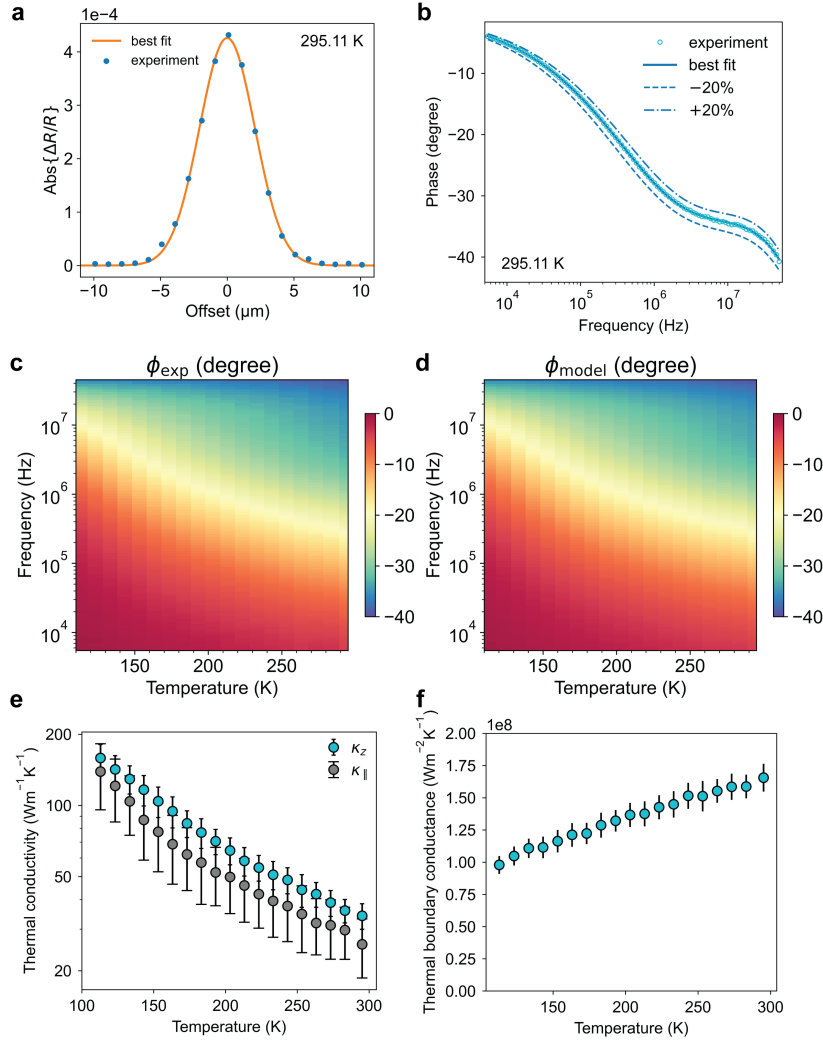


Fig. S15 | Characterization of thermal transport in c-cut sapphire using a sputtered gold transducer. **a**, The amplitude of thermoreflectance at 50 MHz as a function of beam offset distance gives an effective beam radius of $r_{\text{eff}} = 2.93 \mu\text{m}$. **b**, The experimental data and the best fit from the heat diffusion model at 295.11 K, where we fit the thermal conductivity components κ_{\parallel} and κ_z and the thermal boundary conductance G . The dashed and dash-dotted lines represent changes of -20% and $+20\%$ in κ_z , respectively. **c,d**, The phase lag data at different temperatures from experiments and best fits show good agreement. The bright stripe that decreases with increasing temperature corresponds roughly to the critical frequency, $\omega_c \sim D/(\pi r_{\text{eff}}^2)$, which distinguishes diffusivity-dominated and effusivity-dominated transport. Here, $D = \kappa/C$ is the thermal diffusivity that decays with temperature in the 100 K to 300 K range due to three-phonon scattering. **e**, The thermal conductivity κ_{\parallel} and κ_z in c-cut sapphire. The error bars are calculated using Monte Carlo simulations assuming a 5% uncertainty in each parameter. **f**, The thermal boundary conductance between the sputtered gold film and sapphire.

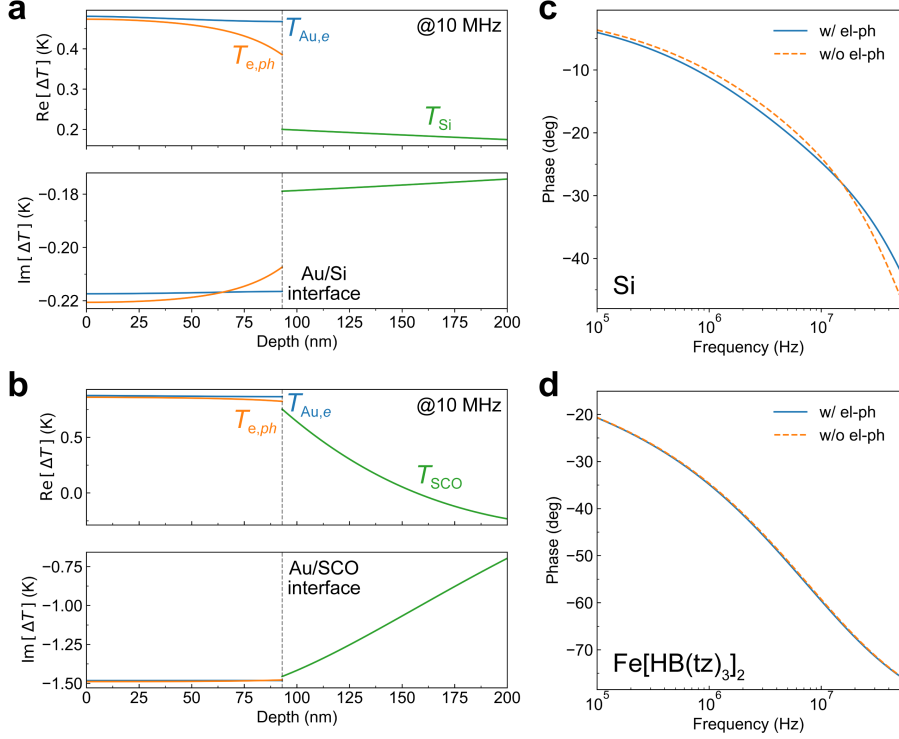


Fig. S16 | Negligible effect of electron-phonon coupling on FDTR signals for Fe[HB(tz)₃]₂.

a,b, Electron and phonon temperature profiles in the Au transducer layer, and the phonon temperatures in the non-metallic substrates: Si (**a**) and Fe[HB(tz)₃]₂ (**b**), at a modulation frequency of 10 MHz. The vertical dashed lines indicate the location of the interface. **c,d,** Calculated phase of thermoreflectance at 295 K for Si (**c**) and Fe[HB(tz)₃]₂ (**d**), with and without considering electron-phonon coupling in the metallic layer. Parameters used: for gold, electronic thermal conductivity $\kappa_{Au,e} = 165 \text{ W m}^{-1} \text{ K}^{-1}$, phonon thermal conductivity $\kappa_{Au,p} = 10 \text{ W m}^{-1} \text{ K}^{-1}$, electronic heat capacity $C_{Au,e} = 2 \times 10^4 \text{ J m}^{-3} \text{ K}^{-1}$, phonon heat capacity $C_{Au,p} = 2.48 \times 10^6 \text{ J m}^{-3} \text{ K}^{-1}$, electron-phonon energy transfer rate coefficient $g = 2 \times 10^{16} \text{ W m}^{-3} \text{ K}^{-1}$; for the substrate, thermal conductivities $\kappa_{Si} = 149 \text{ W m}^{-1} \text{ K}^{-1}$ and $\kappa_{Fe[HB(tz)_3]_2} = 0.85 \text{ W m}^{-1} \text{ K}^{-1}$; thermal boundary conductance $G = 10^8 \text{ W m}^{-2} \text{ K}^{-1}$; and absorbed pump power $P_0 = 0.6 \text{ mW}$. Note that the thermal resistance associated with the extremely thin (2 nm) Ti adhesion layer can be effectively lumped into G , as verified by explicitly modeling this layer. The results show that electron-phonon coupling has a negligible effect on the FDTR signals for Fe[HB(tz)₃]₂, which has a lower thermal conductivity, but plays a more significant role for Si, which has a higher thermal conductivity.

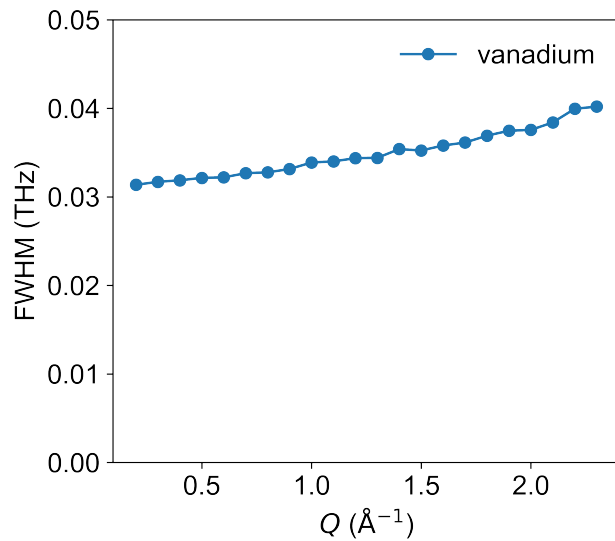


Fig. S17 | Assessment of the instrumental resolution for neutron scattering using a vanadium reference sample. Full width at half maximum (FWHM) as a function of momentum transfer Q in a vanadium reference sample. The FWHM is determined by fitting the neutron scattering function $S(Q,\omega)$ near $\omega = 0$ at a given Q with a Gaussian function, where $\text{FWHM} = 2.3548\sigma$ and σ is the standard deviation of the Gaussian.

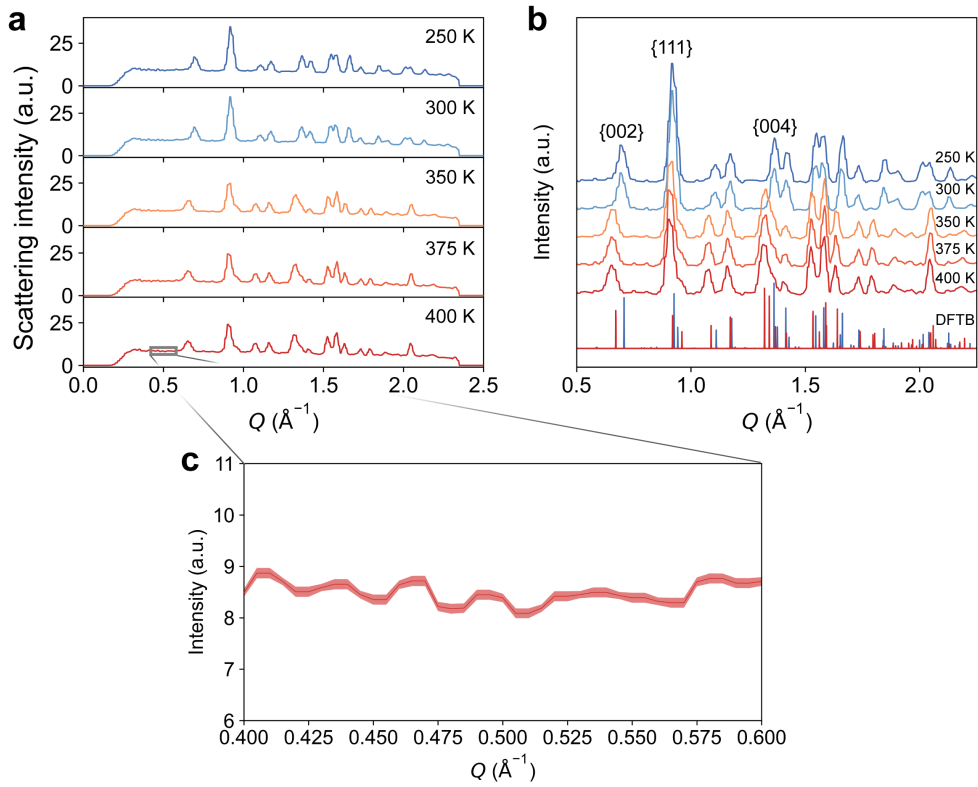


Fig. S18 | Elastic neutron scattering intensity of the LS and HS phases of $\text{Fe}[\text{HB}(\text{tz})_3]_2$. **a**, Temperature-dependent elastic neutron scattering intensity as a function of momentum. The background (baseline) and peaks originate from incoherent scattering and coherent (Bragg) scattering, respectively. The peak intensity is sufficiently high that the presence of background does not obscure peak assignment. **b**, The Bragg scattering intensity shows minor changes across the SCO transition. The blue and red traces at the bottom are the calculated intensity for LS and HS using DFTB-optimized geometry. Across the SCO transition, the unit cell preferably expands along the crystallographic c axis. **c**, Enlarged view of the elastic scattering intensity, with the line width denoting the error bars, which are consistently smaller than 1.6% for Q between 0.5 and 2.25 \AA^{-1} at all temperatures.

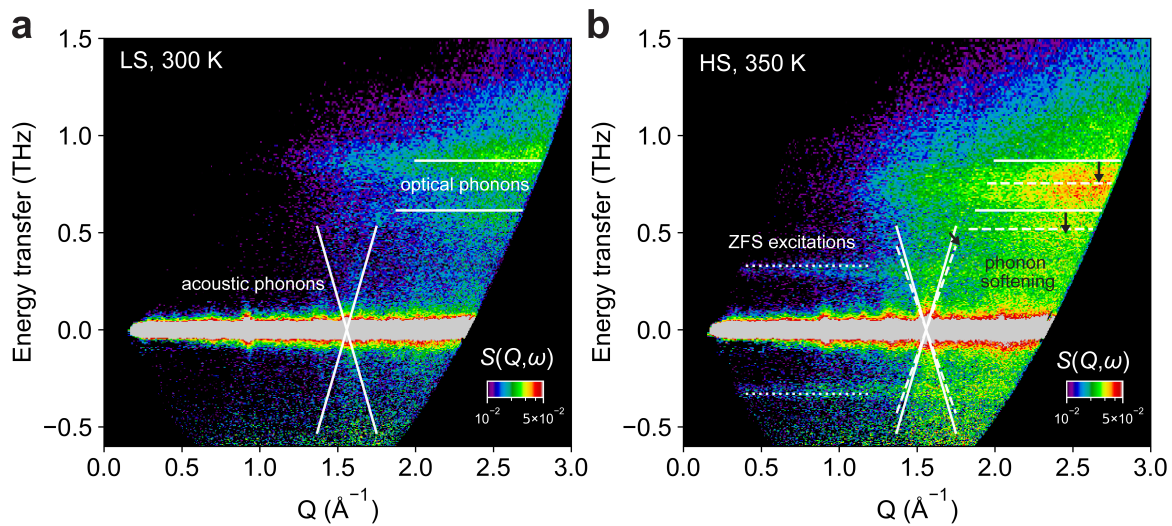


Fig. S19 | The low-energy neutron scattering function, $S(Q, \omega)$, of the LS and HS phases of $\text{Fe}[\text{HB}(\text{tz})_3]_2$. **a**, The acoustic phonons and optical phonons in the LS phase are highlighted with solid lines. **b**, Compared with the LS phase, the acoustic and optical phonons in the HS phase (indicated by dashed lines) undergo phonon softening. Notably, zero-field splitting excitations (dotted lines) are present only in the HS phase. This occurrence is attributed to the paramagnetism arising from unpaired electrons⁸⁴. The energy corresponds to the transition between states with a spin magnetic quantum number $M_s = 0$ and $M_s = \pm 1$, involving energy exchange between an electron and a neutron.

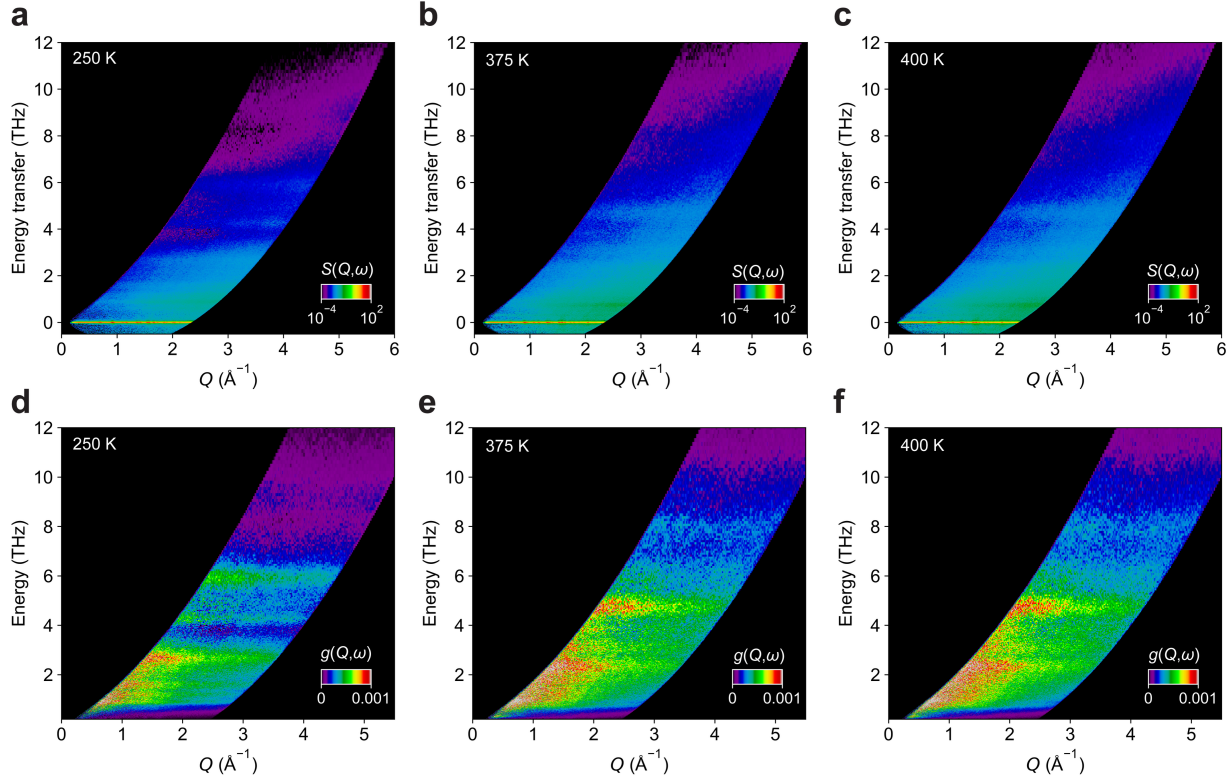


Fig. S20 | The neutron scattering function $S(Q,\omega)$ (a-c) and number of phonon states $g(Q,\omega)$ (d-e) for $\text{Fe}[\text{HB(tz)}_3]_2$ with energy ω and momentum transfer $\hbar Q$ at 250 K, 375 K and 400 K. The bright stripe at zero energy transfer is the elastic neutron scattering function, and the rest is the inelastic neutron scattering function. Combined with the data in Fig. 3 of the main text, we observe that the inelastic neutron scattering function shows remarkable similarity within the same spin state, which highlights the influence of spin state, as opposed to temperature, on vibrational properties.

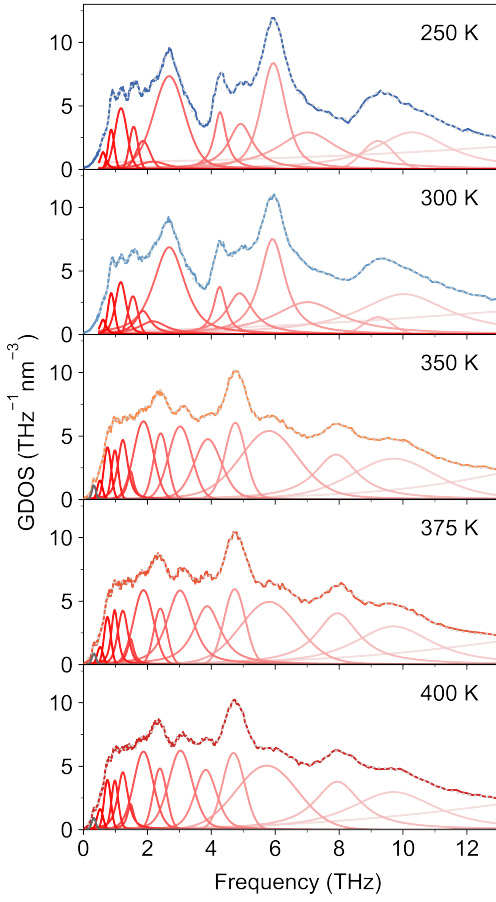


Fig. S21 | Spectral decomposition of the generalized density of states (GDOS). Given the minimal structural change and small volume expansion, we assume that the phonon dispersions consistently shift towards lower energy, while the total number of peaks in the phonon DOS remains unchanged from the LS to the HS phase. Ideally, phonon peaks can be well described by Lorentzian functions. However, the peaks are convoluted with Gaussian-like instrumental resolution (Fig. S17) and further broadened by sample inhomogeneities such as grain boundaries in our powder sample, so a pseudo-Voigt function, which is a linear combination of Lorentzian and Gaussian, more realistically captures the mixed lineshape. In the pseudo-Voigt peak fitting of the GDOS, 13 pseudo-Voigt functions were used to represent phonons below 12 THz. The lowest-energy peaks at 375 K and 400 K, shown in blue lines, are attributed to zero-field splitting rather than phonons. One extra pseudo-Voigt function centered at 20.6 THz is used to account for higher-frequency phonons, which contribute minimally to phonon transport. The dashed grey lines correspond to the sum of all pseudo-Voigt functions. The lower energy cutoffs for fitting are 0.48 THz and 0.12 THz for the LS and HS phases, respectively. Below these frequencies, the GDOS has contributions from acoustic phonons, which follow a different functional form ($\text{GDOS}(\omega) \propto \omega^2$) that is not well represented by the pseudo-Voigt function.

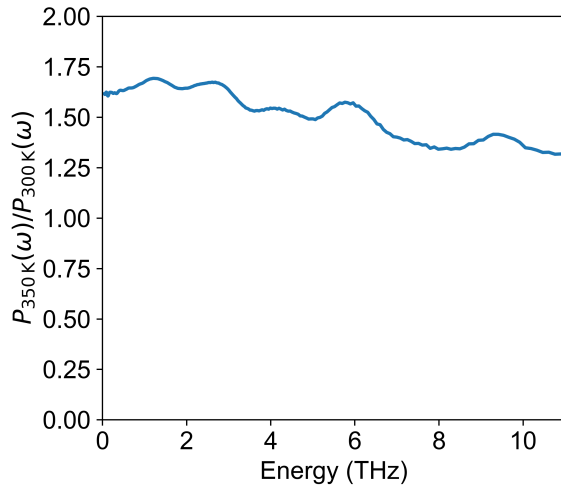


Fig. S22 | Increased three-phonon scattering phase space across the SCO transition. The ratio between the weighted three-phonon scattering phase space (Eq. S42) in the HS (350 K) and LS (300 K) phases of Fe[HB(tz)₃]₂. The three-phonon scattering phase space below 4 THz is increased by over 1.5 times across the SCO transition, indicating that the phonon lifetime ($\tau \propto P(\omega)^{-1}$) decreases by over a factor of 1.5.

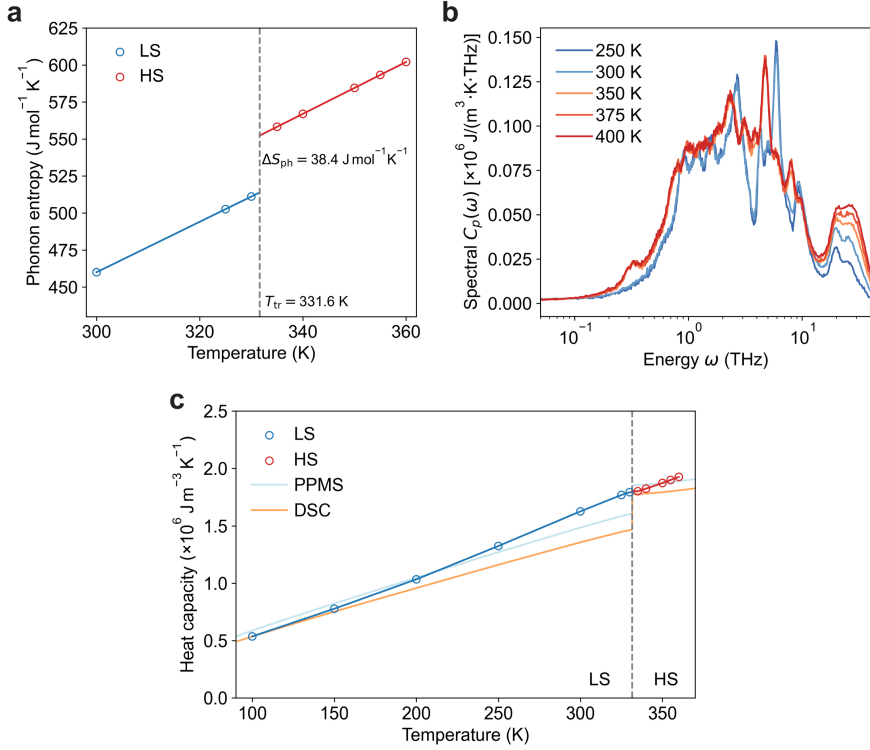


Fig. S23 | The phonon entropy and heat capacity from inelastic neutron scattering. **a**, The phonon entropy under the harmonic approximation is, $S = \frac{1}{2T} \int_0^{\omega_{\text{max}}} \hbar\omega \coth\left(\frac{\hbar\omega}{2k_B T}\right) g(\omega) d\omega - k_B \int_0^{\omega_{\text{max}}} \ln\left(2\sinh\left(\frac{\hbar\omega}{2k_B T}\right)\right) g(\omega) d\omega$, where T is the temperature, $g(\omega)$ is the phonon density of state and ω_{max} is the maximum frequency. We use the GDOS at 300 K and 350 K as the phonon density of states in the LS and HS phases of $\text{Fe}[\text{HB}(\text{tz})_3]_2$, respectively. The circles correspond to the phonon entropy data computed using unit cell volumes from XRD, and the lines correspond to linear fits that can be extrapolated to the phase transition temperature. The change in phonon entropy during the phase transition, read from the discontinuity at the phase transition temperature ($T_{\text{tr}} = 331.6 \text{ K}$), is $\Delta S_{\text{ph}} = 38.4 \text{ J/mol/K}$. This value agrees well with $\Delta S_{\text{ph}} = \Delta S_{\text{DSC}} - \Delta S_{\text{el}} = 33.4 \text{ J/mol/K}$ reported in Fig. 1. **b**, The spectral phonon heat capacity, given by, $C(\omega) = k_B g(\omega) \left(\frac{\hbar\omega}{k_B T}\right)^2 \exp\left(\frac{\hbar\omega}{2k_B T}\right) \left[\exp\left(\frac{\hbar\omega}{2k_B T}\right) - 1\right]^{-2}$, suggests that phonons between 1 THz and 10 THz contribute the most to the heat capacity. We observe pronounced changes in the frequency dependence of the spectral heat capacity across the SCO transition, while within the same spin state, the spectral heat capacity for phonons stays the same except for phonons above 10 THz (simply due to Bose–Einstein statistics). This suggests that the phonon dispersion remains the same within the same spin state and undergoes significant changes when the spin state changes. **c**, The lattice heat capacity, evaluated via $C(T) = \int_0^{\omega_{\text{max}}} C(\omega) d\omega$, agrees reasonably well with the lattice heat capacity determined by PPMS and DSC. The discontinuity in the heat capacity across the SCO transition from inelastic neutron scattering is smaller than for PPMS and DSC. These discrepancies in heat capacity, however, do not significantly impact the optimal fits for thermal conductivity.

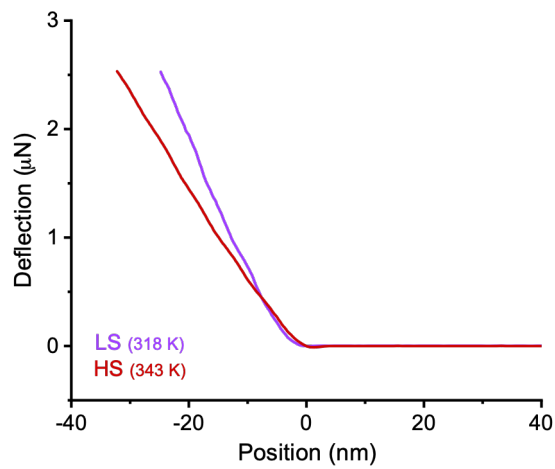


Fig. S24 | Nanoindentation measurements for different spin states of $\text{Fe}[\text{HB}(\text{tz})_3]_2$. The elastic moduli at 318 K and 343 K were found to be 9.2 GPa and 4.6 GPa, respectively. The nanoindentation experiment was performed on a Bruker JPK NanoWizard 4 XP atomic force microscope using a calibrated 32 N/m tip with a quadratic pyramid geometry on a rectangular cantilever. Both force–distance curves were fit using a Hertzian model with identical fitting parameters and tip calibrations.

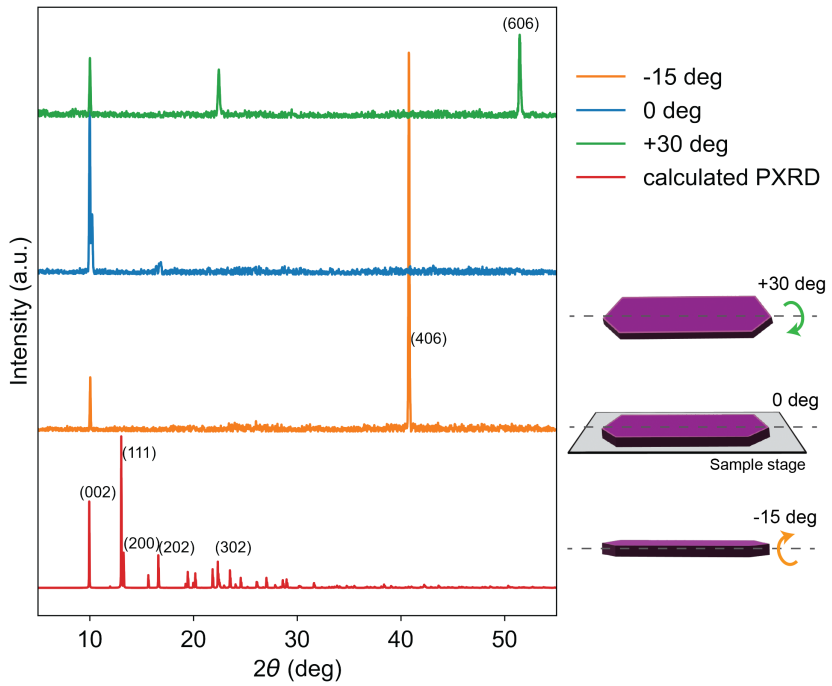


Fig. S25 | Determining the orientation of $\text{Fe}[\text{HB}(\text{tz})_3]_2$ single crystals. Since our FDTR measurement is sensitive only to the cross-plane thermal conductivity, κ_z , we used X-ray diffraction to identify the crystallographic axis of the cross-plane direction. We conducted the single crystal X-ray scattering measurement ($\text{Cu K}\alpha$, $\lambda = 1.54 \text{ \AA}$) using a Bruker D8 DISCOVER X-ray diffractometer equipped with a two-dimensional V500 detector. The crystal sample (purple polyhedron) was deposited on a Si substrate (gray slab), identical to the configuration used in the FDTR measurements. There are two notable features: first, there are no peaks associated with the (010) axis; second, the (002) peak intensity decreases as the angle deviates from 0 deg in either direction. Therefore, we infer that the dashed line (the rotation axis) corresponds to the (010) axis. The planar surface is normal to the (001) axis, while the direction parallel to the Si substrate and perpendicular to the rotation axis corresponds to the (100) axis.

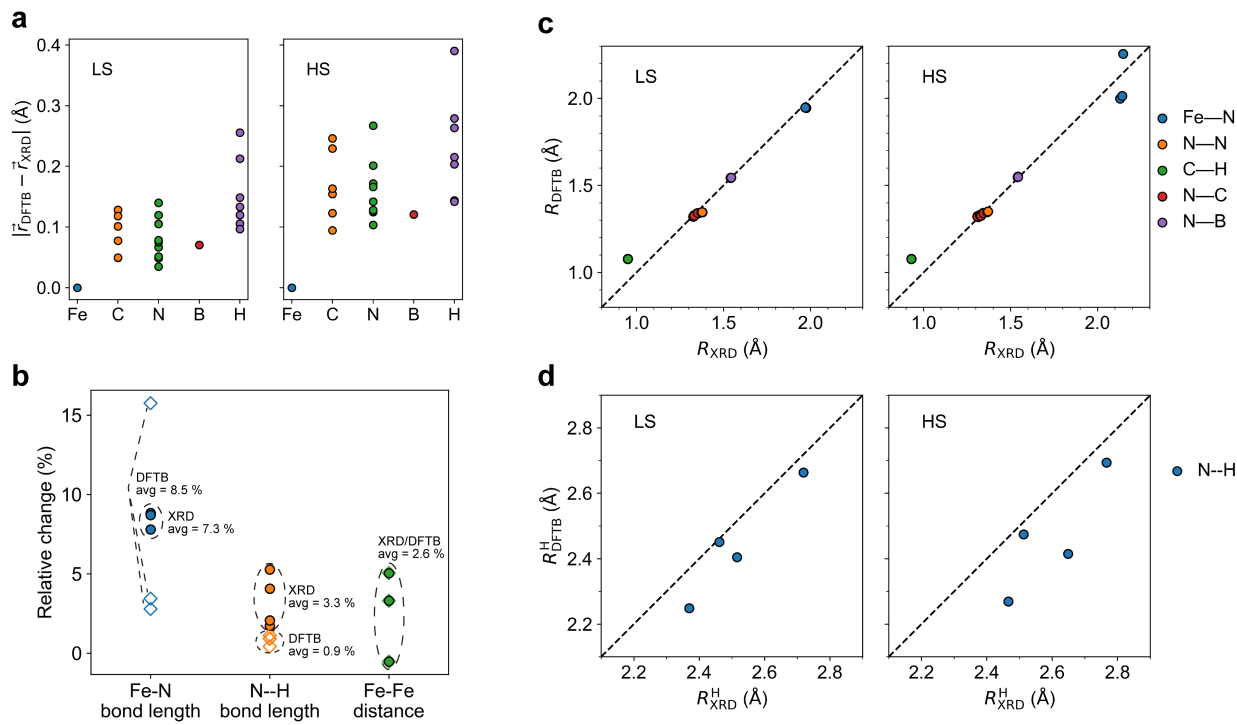


Fig. S26 | DFTB calculations of $\text{Fe}[\text{HB}(\text{tz})_3]_2$ across the SCO transition. **a**, The calculated change in distance of an atom to the Fe atom within an $\text{Fe}[\text{HB}(\text{tz})_3]_2$ molecule in the LS and HS phases. **b**, The change in the intramolecular and intermolecular bond lengths, as well as the Fe-Fe distance between two adjacent molecules from DFTB (open) and XRD (filled), across the SCO transition. **c,d**, The intramolecular (**c**) and intermolecular (**d**) bond lengths in the optimized structure used in the DFTB calculations are in reasonable agreement with those determined by XRD experiments.

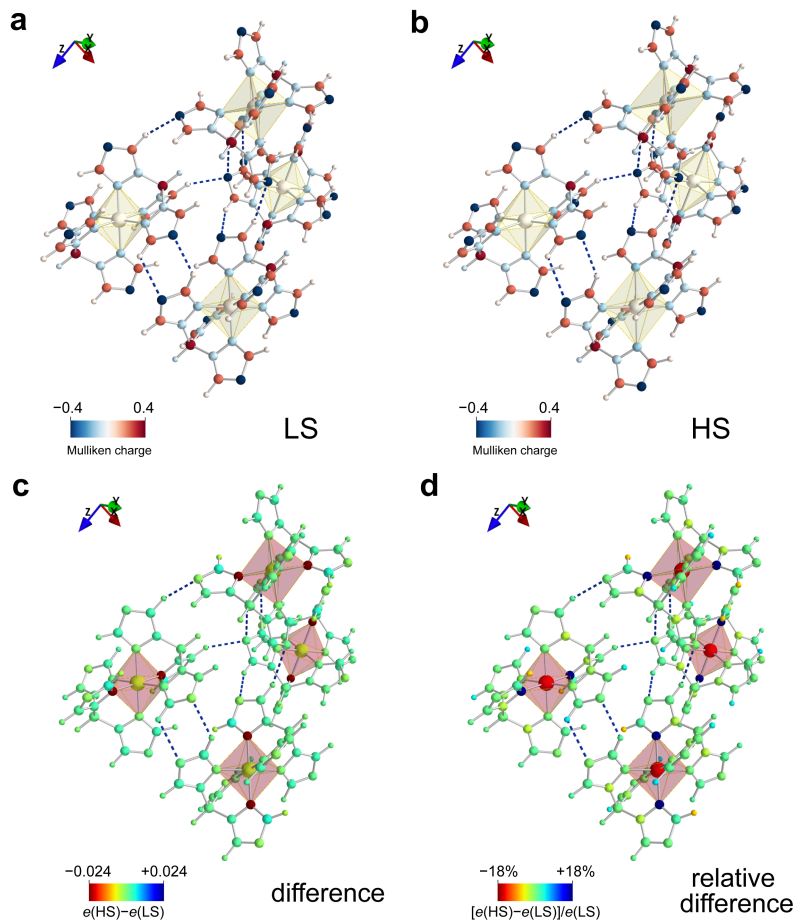


Fig. S27 | Mulliken charge and hydrogen bonding within the unit cell of $\text{Fe}[\text{HB}(\text{tz})_3]_2$ from DFTB calculations. **a,b,** The Mulliken population, defined as the sum of the populations in all atomic basis functions associated with the same atom and represented by color, shown for both LS (**a**) and HS (**b**) phases. Hydrogen bonds between positively charged H atoms and negatively charged N atoms are marked by navy blue dashed lines. **c,d,** Difference and relative change in Mulliken charges between the HS [$e(\text{HS})$] and LS [$e(\text{LS})$] phases. We observe small differences in Mulliken charges between the LS and HS phases (with magnitudes smaller than 0.024 elementary charge), which would induce small changes in the hydrogen bonding interactions (Fig. 4b). Notably, these changes break the D_{3d} symmetry of the molecule (e.g., 2 of the 6 N atoms that directly bonded to Fe become 18% less negatively charged). This symmetry lowering might lift certain constraints on atomic motions and reduce the corresponding restoring forces, which contributes to the softening of specific phonon modes.

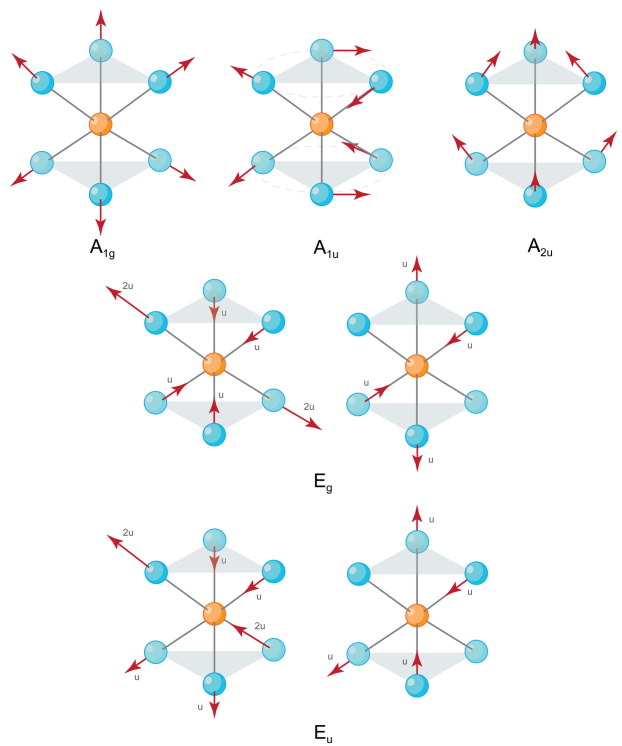


Fig. S28 | Vibrational modes of a generic D_{3d} molecule. The polyhedron formed by the metal and surrounding ligands undergoes different types of deformation/distortion under vibrational modes of different irreducible representations. The letter “u” stands for an arbitrary unit length. For instance, for an A_{1g} vibrational mode, the metal-ligand bonds all elongate by the same distance, and thus all angles of neighboring metal-ligand bonds remain the same. In this case, the polyhedron is not distorted. In contrast, for an A_{1u} mode, the top half and bottom half of ligands rotate with respect to the C_3 rotation symmetry axis in opposite directions, while the metal-ligand bond lengths remain unaltered. As a result, the angles between adjacent metal-ligand bonds are changed. For the E_g mode, the metal-ligand bonds along one particular axis becomes much longer than other axes, which changes the mean and variance of the six metal-ligand bonds. By examining the distinctive and shared features of these irreducible representations, we can categorize the normal modes of a single $\text{Fe}[\text{HB(tz)}_3]_2$ molecule into three types of deformation that changes the polyhedron associated with bonding Fe and N atoms (see Fig. S29).

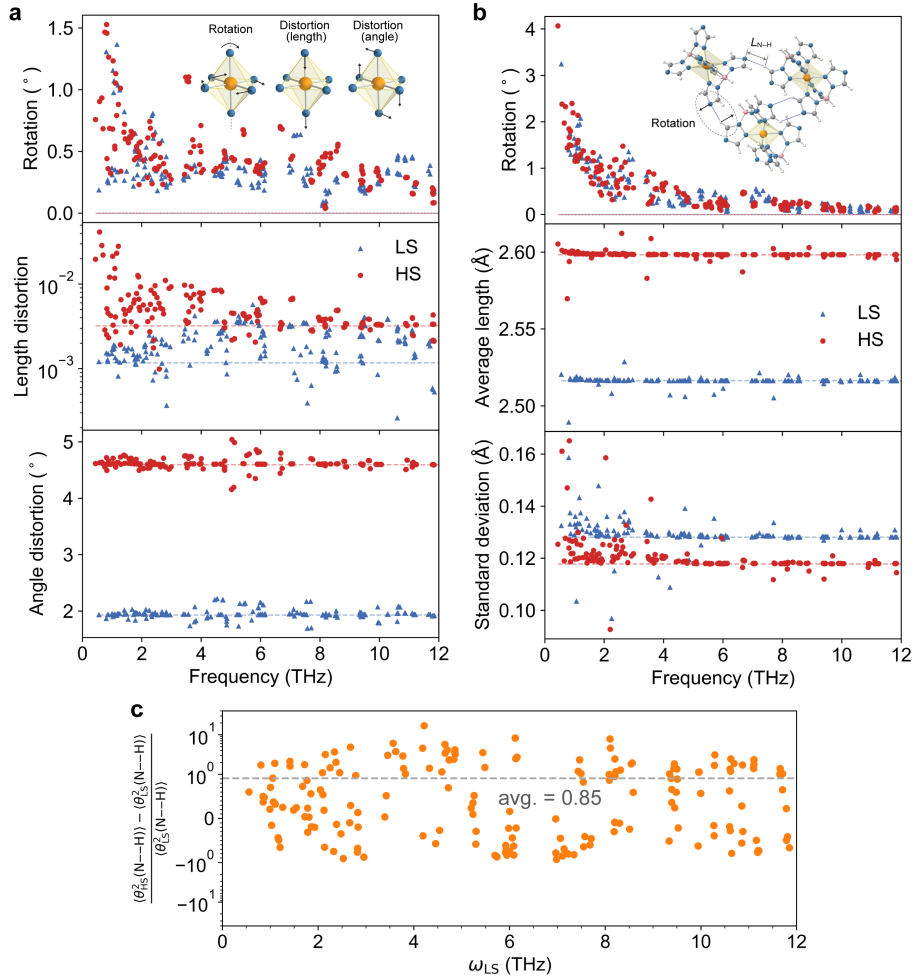


Fig. S29 | Structural changes due to intramolecular and intermolecular vibrational modes in the LS and HS phases of $\text{Fe}[\text{HB}(\text{tz})_3]_2$. **a**, The rotation, length distortion and angle distortion of the Fe-N polygon by different phonon modes. The dashed lines refer to the case of the atomic structure at equilibrium (no phonon excited). The inset shows three possible vibrational modes corresponding to three types of distortion. The orange and blue spheres correspond to Fe and N atoms, respectively. **b**, The rotation, average length and standard deviation of N---H hydrogen bonds. In the inset, a possible pattern of N---H bond rotation is shown. The length of one of the N---H hydrogen bonds is marked. The dashed lines correspond to the structure without any phonon excitation. Note that in the ideal atomic structure at equilibrium, the N---H hydrogen bond lengths are not the same, hence the dashed lines in the bottom panel are non-zero. **c**, The relative increase of mean squared angular displacements of N---H bonds from optical phonons upon transition from the LS phase to the HS phase, reflecting the enhanced amplitude of libration modes in the HS state. The average relative enhancement for optical phonons below 12 THz is 85%. Calculations for both the LS and HS phases were performed at the phase transition temperature $T_{\text{tr}} = 331$ K.

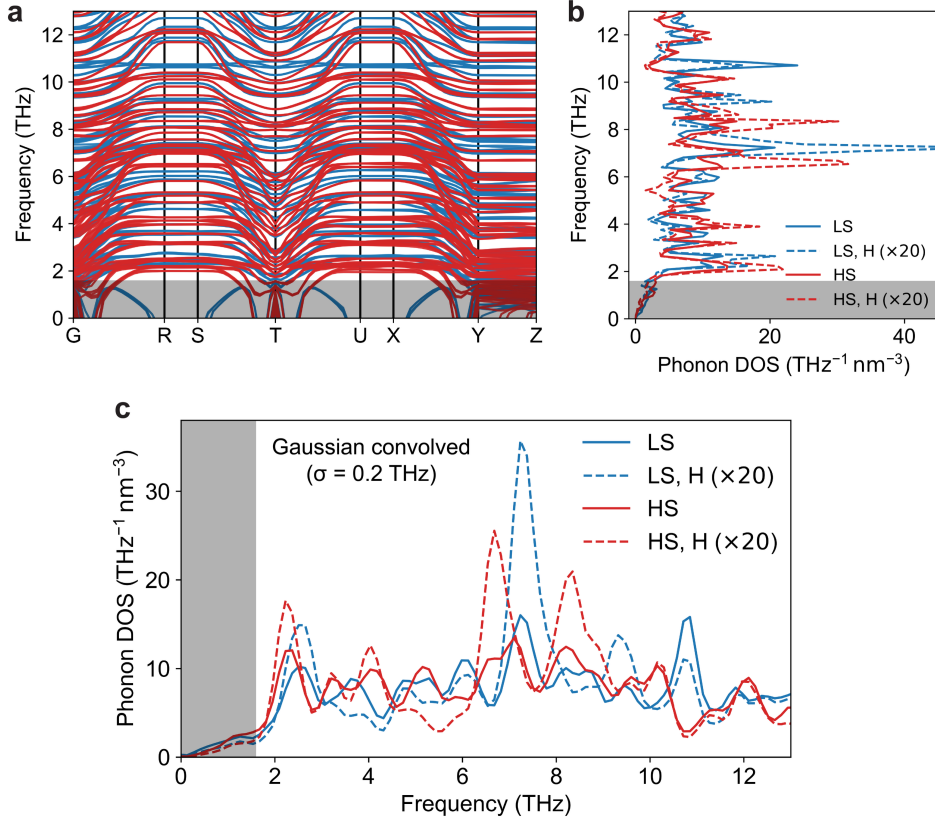


Fig. S30 | Lattice dynamics in the LS and HS phases of $\text{Fe}[\text{HB}(\text{tz})_3]_2$ calculated by DFTB. **a**, Phonon dispersion curves along high-symmetry paths in the 1st Brillouin zone for the LS (blue lines) and HS (red lines) phases. Note that the calculated phonon dispersion relations below 1.6 THz may not accurately represent the lattice dynamics, as these phonon modes exhibit imaginary frequencies at certain \mathbf{q} points within the 1st Brillouin zone (indicated by grey shading). **b**, Total and hydrogen-projected phonon density of states, computed using a $50 \times 50 \times 50$ \mathbf{q} -point mesh and Gaussian width of 0.05 THz for the delta function. **c**, Phonon densities of states after convolution with a Gaussian with a standard deviation of 0.2 THz. We observe red shifts of phonon peaks in calculated phonon density of states from the LS to HS phases, consistent with the inelastic neutron scattering data (see Fig. 3).

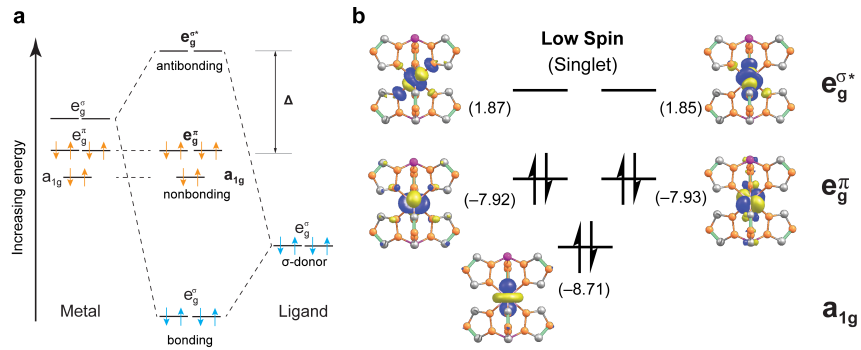


Fig. S31 | The molecular energy levels and orbitals of $\text{Fe}[\text{HB}(\text{tz})_3]_2$. **a**, The molecular orbital diagram for a $\text{Fe}[\text{HB}(\text{tz})_3]_2$ molecule. From symmetry analysis, the d orbitals of the transition metal ion in a trigonal-antiprismatic complex split into e_g^σ ($\frac{\sqrt{3}}{3}d_{x^2-y^2} - \frac{\sqrt{6}}{3}d_{xz}$, $\frac{\sqrt{3}}{3}d_{xy} + \frac{\sqrt{6}}{3}d_{yz}$), e_g^π ($\frac{\sqrt{3}}{3}d_{yz} - \frac{\sqrt{6}}{3}d_{xy}$, $\frac{\sqrt{3}}{3}d_{xz} + \frac{\sqrt{6}}{3}d_{x^2-y^2}$), and a_{1g} (d_{z^2}). Note that the d-orbitals are defined in the Cartesian coordination system where the z-axis aligns with the C_3 rotational (B-Fe-B) axis. **b**, The energy levels (in unit of eV) and wavefunctions in the LS phase from DFT calculations, where probability density value of 0.05 a.u. was used in the isosurface plot.

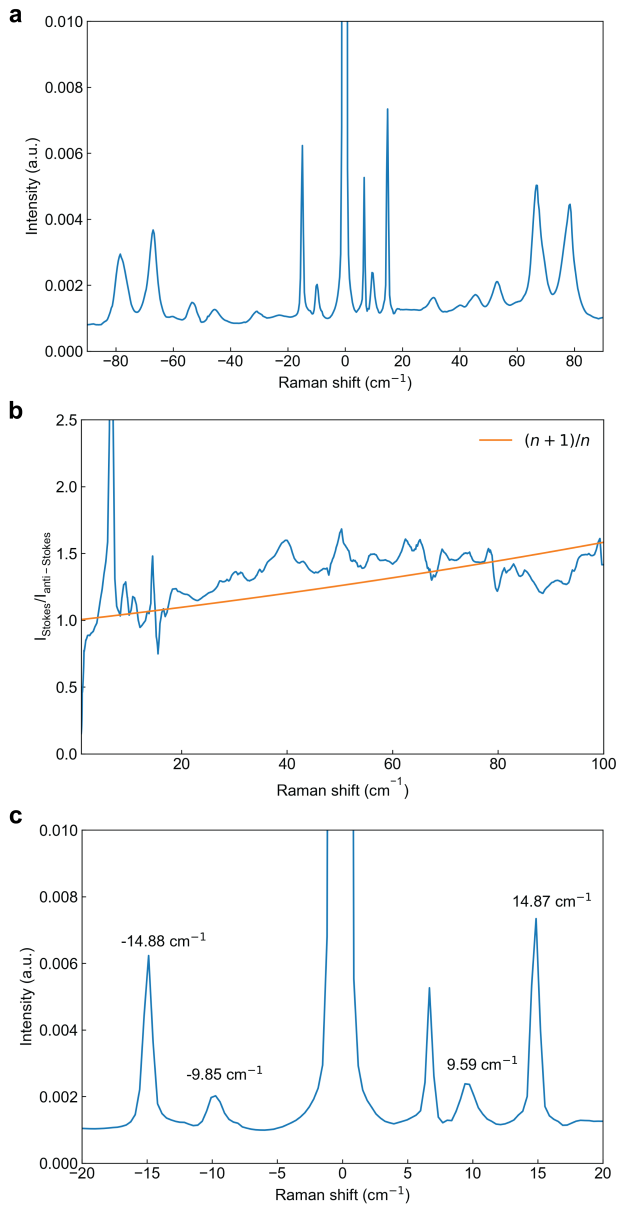


Fig. S32 | The Raman spectrum of L-cysteine at room temperature. **a**, The full Raman spectrum of L-cysteine including Stokes and anti-Stokes Raman scattering. **b**, The ratio of Stokes scattering intensity and anti-Stokes scattering intensity (blue line) in comparison with $(n+1)/n$, where n is the Bose-Einstein distribution function. **c**, The low-frequency region of the Raman spectrum of L-cysteine.

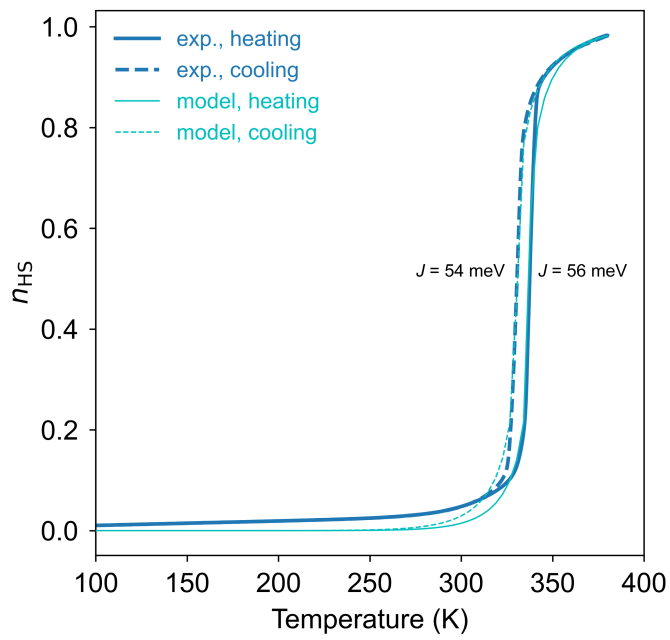


Fig. S33 | Modeling the SCO transition in $\text{Fe}[\text{HB}(\text{tz})_3]_2$. The fraction of HS Fe centers from SQUID measurements (thick lines) and modeling using fitted parameters (thin lines) show a reasonable match. Solid lines and dash lines correspond to heating and cooling processes, respectively. The interaction constants were found to be 54 meV and 56 meV for cooling and heating processes, respectively.

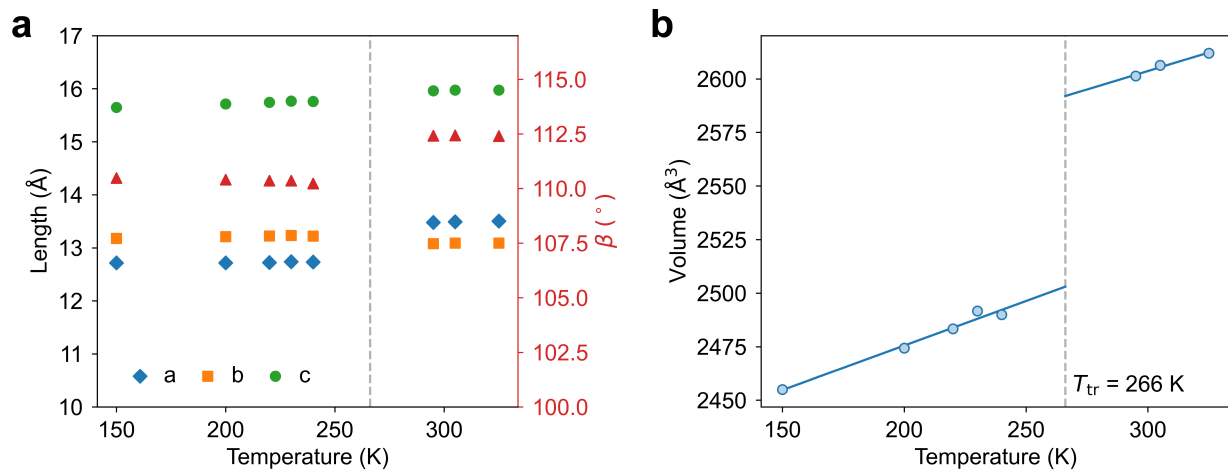


Fig. S34 | Temperature-dependent unit-cell parameters of $\text{Fe}(\text{Fpr-trz}_2\text{-dmpn})(\text{NCS})_2$. **a**, Lattice parameters a , b , c and monoclinic angle β as a function of temperature. **b**, Unit-cell volume in the LS (circles left of dashed line) and HS (circles right) phases. Linear fits are conducted separately for each phase and extrapolated to $T_{\text{tr}} = 266 \text{ K}$ (indicated by the vertical dashed line).

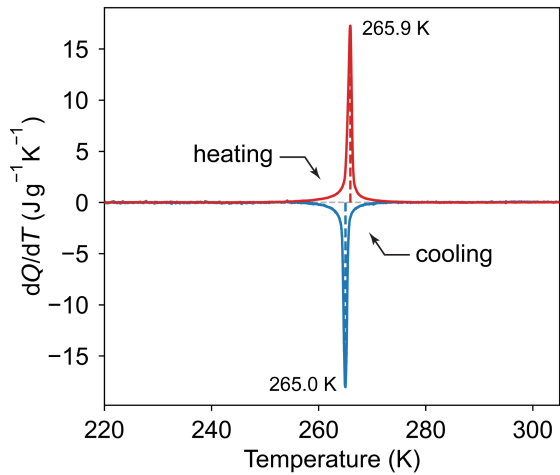


Fig. S35 | Differential scanning calorimetry of $\text{Fe}(\text{Fpr-trz}_2\text{-dmpn})(\text{NCS})_2$. The heating and cooling rates are set at 1 K min^{-1} . Heating (red) and cooling (blue) DSC traces were obtained by subtracting the measured data with cubic spline baselines. The corresponding peak temperatures are marked by vertical dashed lines. The entropy change during the heating-induced SCO transition, presented in Fig. 5c, was obtained by $\Delta S(T) = \Delta H(T)/T_{\text{tr}}$.

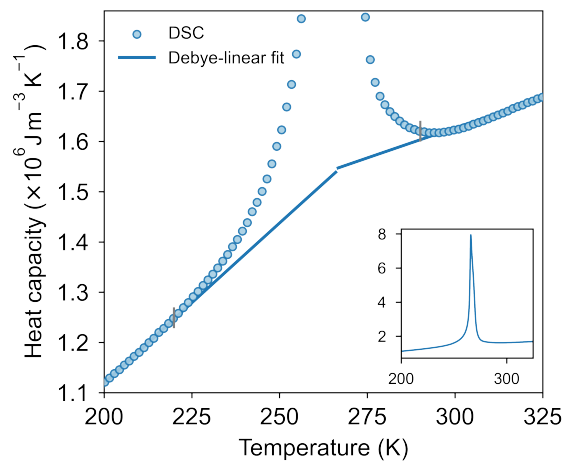


Fig. S36 | Volumetric heat capacity of $\text{Fe}(\text{Fpr-trz}_2\text{-dmpn})(\text{NCS})_2$. Circles: heat capacity from measured by DSC. Lines: best-fit Debye-linear models for the LS and HS phases, respectively. Inset: full DSC heat capacity data.

Table S1. Crystallographic information for Fe(Fpr-trz₂-dmfpn)(NCS)₂

	240 K	285 K
Formula	$\text{C}_{19}\text{H}_{26}\text{F}_2\text{FeN}_{10}\text{S}_2$	$\text{C}_{19}\text{H}_{26}\text{F}_2\text{FeN}_{10}\text{S}_2$
Formula weight (g/mol)	552.47	552.47
Wavelength, λ (Å)	0.71073	0.71073
Temperature (K)	240	285
Crystal System	Monoclinic	Monoclinic
Space Group	$P2_1/c$	$P2_1/c$
a (Å)	12.7271(4)	13.4595(4)
b (Å)	13.2273(4)	13.0751(4)
c (Å)	15.7554(4)	15.9457(4)
α (°)	90	90
β (°)	110.2860(10)	112.382(1)
γ (°)	90	90
Volume (Å ³)	2487.83(13)	2594.79(13)
Z	4	4
Density (g/cm ³)	1.475	1.414
Crystal color	Dark red	Light reddish-orange
Crystal size (mm)	0.15×0.018×0.31	0.13×0.19×0.28
Absorption correction	Multi-scan	Multi-scan
Absorption coefficient, μ (mm ⁻¹)	0.818	0.784
F_{000}	1144	1144
2θ range (°)	2.356 to 29.578	3.031 to 49.315
(h , k , l) _{max}	17, 18, 21	16, 16, 19
Reflections collected	93396	53971
Independent reflections	6943	5277
Completeness to θ_{max}	0.994	0.993
R_{int}	0.0239	0.0284
Data / restraints / parameters	6943 / 0 / 325	5277 / 0 / 309
Goodness-of-fit on F^2 ^a	1.027	1.041
R_1 , wR_2 indices [$I > 2\sigma(I)$ data] ^b	0.0336, 0.0887	0.0447, 0.1213
R_1 , wR_2 indices (all data)	0.0379, 0.0919	0.0499, 0.1253
Largest diff. peak and hole	0.806 and -0.468	0.827 and -0.399

^a $\text{GooF} = [\sum[w(F_o^2 - F_c^2)^2] / (n-p)]^{1/2}$ where n is the number of reflections and p is the total number of parameters refined. ^b $R_1 = \sum[|F_o| - |F_c|] / \sum|F_o|$; $wR_2 = [\sum[w(F_o^2 - F_c^2)^2] / \sum[w(F_o^2)^2]]^{1/2}$

Table S2. Thermal conductivity of selected materials below and above the phase transition temperature

Material	κ_{LT} (W m ⁻¹ K ⁻¹)	κ_{HT} (W m ⁻¹ K ⁻¹)
C ₆₀	0.52	0.39
[Co ₆ Se ₈][C ₆₀] ₂	0.36	0.27
Ni-Mn-In	7.2	12
VO ₂ film	3.5	5.5
VO ₂ nanowire	5.6	5.9
Ge ₂ Sb ₂ Te ₅	1.6	4.8
Hg	0.28	0.069
H ₂ O	2.2	0.56
CaCl ₂ ·6H ₂ O	1.1	0.54
Ba(OH) ₂ ·8H ₂ O	1.3	0.65
MgCl ₂ ·6H ₂ O	0.70	0.57
paraffin wax	1.0	0.67
<u>polyethylene nanofiber*</u>	~11	~1.1

*Estimated from thermal conductance measurement.